Geophysical Journal International

Geophys. J. Int. (2016) **204,** 21–38 doi: 10.1093/gji/ggv437
GJI Marine geosciences and applied geophysics

Bayesian inversion of marine controlled source electromagnetic data offshore Vancouver Island, Canada

Romina A.S. Gehrmann,[1,2] Katrin Schwalenberg,[2] Michael Riedel,[1,3,*] George D. Spence,[1] Volkhard Spieß[4] and Stan E. Dosso[1]

[1] *School of Earth and Ocean Sciences, University of Victoria, Victoria, BC, Canada. E-mail: rominagehrmann@hotmail.com*
[2] *Federal Institute for Geosciences and Natural Resources, Hannover, Germany*
[3] *Geological Survey of Canada, Sidney, BC, Canada*
[4] *Faculty of Geosciences, University of Bremen, Bremen, Germany*

Accepted 2015 October 6. Received 2015 October 6; in original form 2015 June 2

SUMMARY

This paper applies nonlinear Bayesian inversion to marine controlled source electromagnetic (CSEM) data collected near two sites of the Integrated Ocean Drilling Program (IODP) Expedition 311 on the northern Cascadia Margin to investigate subseafloor resistivity structure related to gas hydrate deposits and cold vents. The Cascadia margin, off the west coast of Vancouver Island, Canada, has a large accretionary prism where sediments are under pressure due to convergent plate boundary tectonics. Gas hydrate deposits and cold vent structures have previously been investigated by various geophysical methods and seabed drilling. Here, we invert time-domain CSEM data collected at Sites U1328 and U1329 of IODP Expedition 311 using Bayesian methods to derive subsurface resistivity model parameters and uncertainties. The Bayesian information criterion is applied to determine the amount of structure (number of layers in a depth-dependent model) that can be resolved by the data. The parameter space is sampled with the Metropolis–Hastings algorithm in principal-component space, utilizing parallel tempering to ensure wider and efficient sampling and convergence. Nonlinear inversion allows analysis of uncertain acquisition parameters such as time delays between receiver and transmitter clocks as well as input electrical current amplitude. Marginalizing over these instrument parameters in the inversion accounts for their contribution to the geophysical model uncertainties. One-dimensional inversion of time-domain CSEM data collected at measurement sites along a survey line allows interpretation of the subsurface resistivity structure. The data sets can be generally explained by models with 1 to 3 layers. Inversion results at U1329, at the landward edge of the gas hydrate stability zone, indicate a sediment unconformity as well as potential cold vents which were previously unknown. The resistivities generally increase upslope due to sediment erosion along the slope. Inversion results at U1328 on the middle slope suggest several vent systems close to Bullseye vent in agreement with ongoing interdisciplinary observations.

Key words: Probability distributions; Marine electromagnetics; Continental margins: convergent; North America; Pacific Ocean.

1 INTRODUCTION

Marine controlled source electromagnetic (CSEM) methods are applied to evaluate the electrical properties of marine sediments. The electrical resistivity of seafloor sediments, and its reciprocal, conductivity, depend mainly on the sediment porosity and the electrical resistivity of the pore fluid. Therefore, marine CSEM is sensitive to resistive material in the pore spaces such as free gas, oil and gas hydrates. Marine CSEM methods have become a promising tool for offshore hydrocarbon exploration (Ellingsrud *et al.* 2002; Constable & Srnka 2007; Constable 2010). Edwards (1997) proposed the use of marine CSEM for the evaluation of submarine gas hydrates, and the first surveys were conducted on the Northern Cascadia Margin using a time-domain, electric dipole–dipole system (Yuan & Edwards 2000; Schwalenberg *et al.* 2005). Other case studies followed to evaluate gas hydrates at, among others, Hydrate Ridge offshore Oregon, USA, (Weitemeyer *et al.* 2011), the Hikurangi margin offshore New Zealand (Schwalenberg *et al.* 2010a,b), the Gulf of Mexico (Weitemeyer & Constable 2010) and offshore

*Now at: GEOMAR - Helmholtz Centre for Ocean Research Kiel, Germany.

Svalbard (Goswami *et al.* 2013) using both frequency- and time-domain CSEM systems.

The marine CSEM method is based on the diffusion of electromagnetic fields through the resistive subsurface and conductive seawater. Direct interpretation is only possible to a limited extent. To estimate a multilayer resistivity model of the subsurface from CSEM data requires advanced inversion algorithms. Most of the studies mentioned above invert CSEM data with linearized techniques (e.g. Occam's inversion, Constable *et al.* 1987). However, to rigorously estimate uncertainties for model parameters and address the non-uniqueness of CSEM data, we apply a nonlinear Bayesian inversion. Bayesian methods have been implemented by, for example, Hoversten *et al.* (2006) and Chen *et al.* (2007), who jointly inverted CSEM and seismic (amplitude variation with angle of incidence) data for oil and gas saturation, and Buland & Kolbjørnsen (2012), who inverted inline as well as broadside electric and magnetic components of CSEM and magnetotelluric data to solve for resistivities of hydrocarbon reservoirs. Bayesian inversion can be implemented to estimate model parameter uncertainties, and to include additional information (e.g. electric and magnetic components, prior knowledge about subsurface parameters, joint inversion with other geophysical data) to decrease the uncertainties. This is important to interpret the subsurface model accurately. A challenge is to estimate the number of parameters (e.g. resistivity layers) that can be resolved with the data. Too many unknowns cause the problem to be underdetermined and spurious structure might be introduced, while including too few parameters into the inversion may cause model structure to stay unresolved, and uncertainties to be underestimated. Recently, Ray & Key (2012) and Gehrmann *et al.* (2015) have implemented a trans-dimensional Bayesian inversion for marine CSEM data where the number of layers that can be resolved with the data is an unknown in the inversion. Alternatively, Gunning *et al.* (2010) considered effective correlation lengths, a Bayesian smoothing similar to regularization in linearized methods and the Laplace approximation to the Bayesian evidence to estimate the maximum *a posteriori* model (which maximizes the posterior probability density, PPD, and represents the most probable model). Here, we determine the optimal number of subsurface layers using the Bayesian information criterion (BIC) which can be a simpler and less-computationally expensive approach. Computation efficiency is further improved carrying out sampling of the PPD over the model space using the Metropolis–Hastings algorithm in principal-component space (i.e. the parameter space is rotated to minimize the effects of interparameter correlations) to estimate the PPD. Correlated data errors, which are important when estimating the amount of subsurface structure, are addressed here with a non-diagonal data covariance matrix estimated from residual analysis (e.g. Dosso & Dettmer 2011), which has been shown to be appropriate for CSEM data inversion (e.g. Ray *et al.* 2013b; Gehrmann *et al.* 2015).

The marine time-domain CSEM data sets analysed in this study were acquired in the late summers of 2005 and 2006 with a seafloor-towed, horizontal, electric dipole-dipole system (Schwalenberg *et al.* 2005). The two survey areas are located on the middle and upper slope of the continental margin off Vancouver Island, Canada (see Fig. 1). The Northern Cascadia margin is an active subduction zone, where the oceanic Juan de Fuca plate subducts beneath the North American plate. Most of the oceanic sediments are accreted onto the continental margin, pressurized and faulted (Davis & Hyndman 1989). Ongoing fluid flow and localized cold vents have been investigated using heat flow, seismic and borehole data (Davis *et al.* 1990; Hyndman *et al.* 1993; Riedel *et al.* 2009). Gas hydrate occurrences have been detected during various expeditions with geophysical and geochemical techniques (Hyndman & Spence 1992; Yuan *et al.* 1999; Riedel *et al.* 2006b; Dash & Spence 2011). For example, a distinct seismic signature of sediments containing gas hydrates is the bottom simulating reflector (BSR). The BSR generally results from an impedance contrast at the base of the gas hydrate stability zone (GHSZ) caused by free gas beneath the base of the GHSZ (Hyndman & Spence 1992). Seismic surveys and deep sea drilling have indicated possible ways of gas hydrate distributions in marine sediments. For example, gas hydrates have been found to accumulate at the base of the GHSZ (possible mechanism: gas hydrate recycling) as well as in sand layers. Gas hydrates have also been found laterally variable, accumulating within fractures along major fluid conduits (Riedel *et al.* 2006a; Haacke *et al.* 2007; Zühlsdorff & Spiess 2004). While drilling provides very localized, fine-scaled

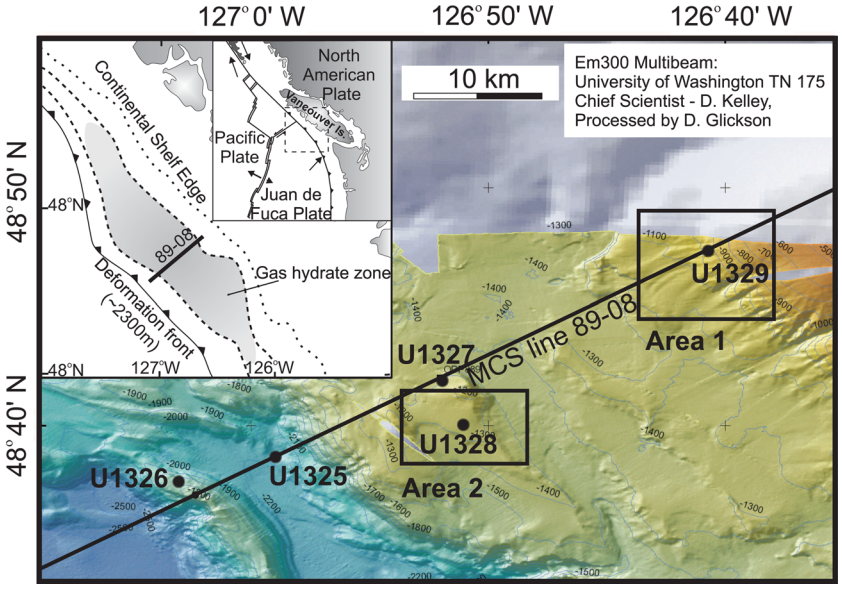

Figure 1. Overview of the Northern Cascadia margin offshore Vancouver Island with multichannel seismic line 89-08 (black line), CSEM survey areas (black rectangles) and location of IODP X311 Sites.

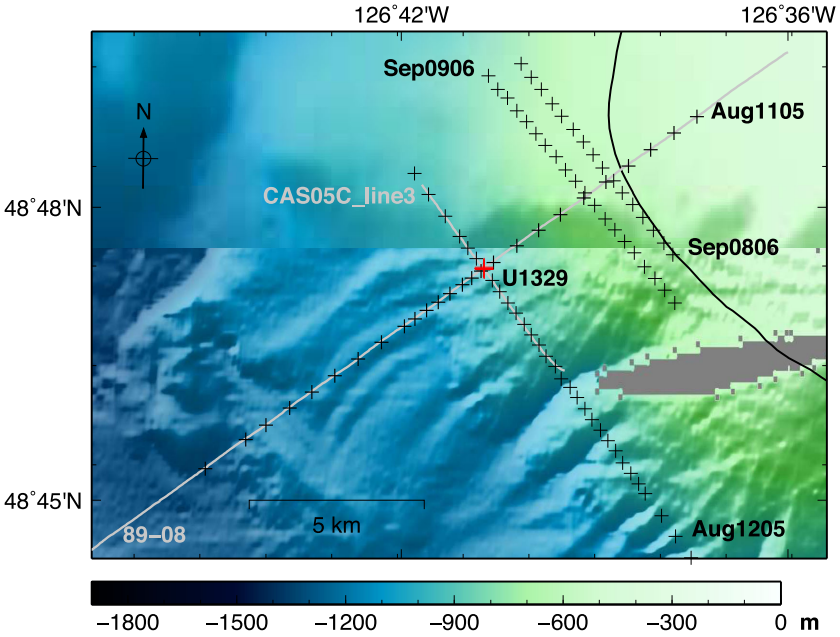

Figure 2. Bathymetry of Area 1 with CSEM way points (black crosses), IODP X311 Site U1329 (red cross), MCS line PGC89-08 and SCS line CAS05C-line3 (grey lines), and estimated landward edge of the GHSZ (black curved line). Grey area on the lower right indicates missing bathymetry data.

information and seismic data are usually sensitive to impedance contrasts associated with velocity and/or density changes, electromagnetic studies allow the evaluation of bulk volumes of sediments containing gas hydrates and/or free gas (Edwards *et al.* 2010). Yuan & Edwards (2000) and Schwalenberg *et al.* (2005) have shown that the CSEM method may detect gas hydrate on the slope (even in absence of a BSR) and at vent systems.

2 GEOLOGY OF THE SURVEY AREAS

A geological interpretation of the survey areas is drawn from the Integrated Ocean Drilling Program (IODP) Expedition 311 (X311) by Expedition 311 Scientists (2005) and Riedel *et al.* (2006a). The two CSEM survey areas are located on the upper slope around X311 Site U1329 (Area 1), and on the middle slope, around the Bullseye vent and Site U1328 (Area 2) as shown in Fig. 1.

2.1 Area 1: upper slope near U1329

Site U1329 is situated 65 km from the west coast of Vancouver Island, Canada, at the upslope edge of the GHSZ. The area is marked with multiple canyons and topographic changes from 500 to 1300 m water depth along a 7.5 km track with an average slope of 6°. Reflection seismic data reveal turbidite sequences and erosional surfaces (Expedition 311 Scientists 2005; Scherwath *et al.* 2006). The detailed analyses at Site U1329 [drilled to ∼220 meters below seafloor (mbsf)] reveal three main lithostratigraphic units (Riedel *et al.* 2006a). Units 1 and 2 consist of Holocene to Pleistocene clay to silty clay to ∼140 mbsf. Diatoms in Unit 2 were dated between >0.3 and 2 Ma. However, Unit 3 consists of late Miocene material (>6.7 Ma) marking the boundary between Units 2 and 3 as an erosional unconformity (Expedition 311 Scientists 2006b), which can also be observed on MCS line 89-08 (see Section 5.3). Resistivities (measured downhole with the *in situ* GeoVISION high-resolution button deep averaging tool) increase from ∼1 Ωm above ∼170 mbsf to >4 Ωm due to a reduction in sediment porosity.

A BSR is observed on MCS line 89-08 and on single channel seismic (SCS) line CAS05C-3 (which runs perpendicular to MCS line 89-08, see Fig. 2), but does not continue upslope of X311 Site U1329. Borehole data through the GHSZ suggest only a few accumulations of gas hydrates at the base of the GHSZ at Site U1329 at 126 mbsf. Estimates of the gas hydrate saturation at this site based on biogenic gas production incorporating paleo-sedimentation rates also suggest a thin gas hydrate occurrence zone at the bottom of the GHSZ (Malinverno *et al.* 2008).

Four CSEM lines around U1329, which were collected in 2005 and 2006, are shown on Fig. 2, one line perpendicular to the slope (Aug1105) and across the drill site, and three lines parallel to the slope (Aug1205, Sep0806, Sep0906). One slope-parallel line intersects at U1329, the other two lines are located further up the slope at the landward edge of the GHSZ.

2.2 Area 2: middle slope, Bullseye vent

Bullseye vent is an extensively studied cold vent site on the middle slope of the Northern Cascadia margin. Massive gas hydrates were recovered in piston cores in the upper 8 mbsf (Riedel *et al.* 2006b). The vent site, one of a series of blank zones observed in reflection seismic data over a wide range of frequencies (Riedel *et al.* 2002), is characterized by a prominent seismic diffraction produced by a shallow gas hydrate cap. CSEM data collected in 2004 prior to X311 revealed highly anomalous electrical resistivities over Bullseye vent which have been interpreted as sediments with high gas hydrate concentrations (Schwalenberg *et al.* 2005). Local gas plumes were observed in 2006 in the water column with an 18 kHz echo sounder (Willoughby *et al.* 2008), and in 2013 with the multibeam system EM710 (Römer, private communication, 2014). The borehole analysis of U1328 revealed three major lithostratigraphic units down to 300 mbsf. Units 1 to 3 contain Pleistocene sediments (<1.6 Ma) that consist of clay and silty clay interbedded with thin sand layers, with few microfossils. Unit 2 (130–200 mbsf) stands

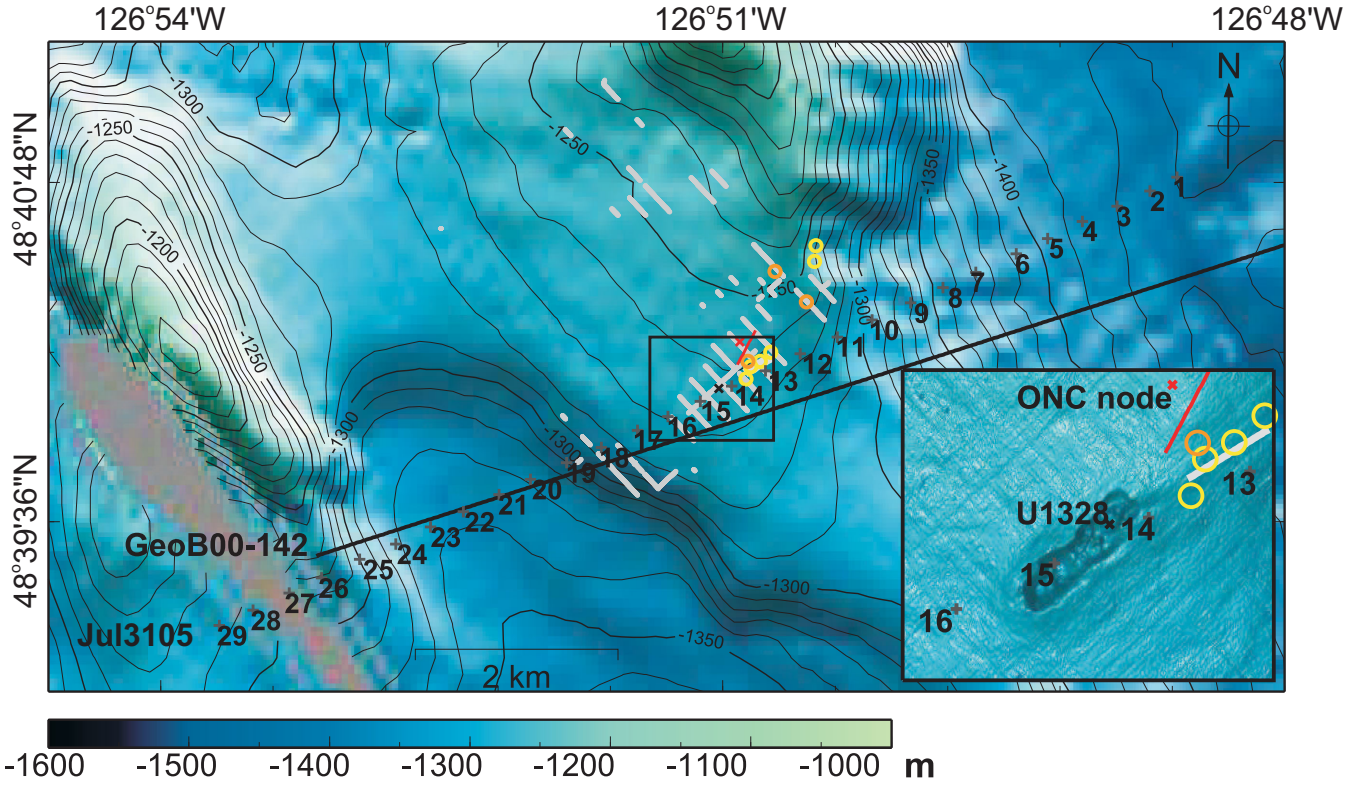

Figure 3. Overview of Area 2 with detailed bathymetry of Bullseye vent in inset (black rectangle) by Paull *et al.* (2009), X311 Site U1328 (black cross), MCS line GeoB00-142 (black line), CSEM WPs (black plus signs) of line Jul3105, Ocean Networks Canada (ONC) platform at Clayoquot Slope (red cross), fixed CSEM system (red line), observed blanking on high-frequency AUV data from Paull *et al.* (2009) (grey lines), observed gas plumes in 2006 on CCGS *John P. Tully* (orange circles) and in 2013 on RV *Falkor* (yellow circles) and bacterial mats observed in 2013 on RV *Falkor* (light grey line on inset). Grey area at lower left indicates missing bathymetry data.

out with a higher abundance of microfossils and smaller content of sand.

Analysis of pore-water chlorinity of sediment cores from U1328 provides information about hydrate formation within the sediment column. Gas hydrate dissociation during recovery causes freshening of the pore water and low chlorinity values, as observed between 150 and 220 mbsf above the base of the GHSZ (especially in the 10 m above the assumed base of the GHSZ at 220 mbsf). However, between 5 and 20 mbsf, high chlorinity values indicate a recent and rapid formation of gas hydrates, faster than the assumed diffusion rate of 5×10^{-6} cm^2 s^{-1} (Riedel *et al.* 2006a). Rapid gas hydrate formation is possible in scenarios of high methane supply, for example, along fractures (Nimblett & Ruppel 2003). Accumulations of resistive material such as gas hydrates are also supported by logging-while drilling (LWD) resistivities of 1 to 20 Ωm between 5 and 50 mbsf (Expedition 311 Scientists 2006a). A strong reflector, possibly related to the top of a solid hydrate cap, is observed on seismic lines just below the seafloor reflection. Chlorinity values and on-board infrared thermal imaging suggest little to no gas hydrate between 60 and 150 mbsf. The lack of gas hydrate at intermediate depths is also supported by low resistivities, which increase with depth from 1 to 2 Ωm between 50 and 150 mbsf. One exception is a thin interval with elevated resistivity of up to 3 Ωm between 90 and 100 mbsf. Hydrates were discovered at 92 mbsf in one core (maximum 38 per cent), but do not seem to be laterally continuous, suggesting hydrate formation along fractures. Free gas concentrations of 58 per cent below the GHSZ were found in one pressure core, but could not be confirmed by wireline acoustic logging or by vertical seismic profiling (Riedel *et al.* 2006a; Expedition 311 Scientists 2006a).

Four CSEM lines were collected across Bullseye vent in 2004 and 2005 (Schwalenberg *et al.* 2005; Schwalenberg 2007). The line analysed here is shown in Fig. 3 and runs in a NE to SW direction intersecting the Bullseye vent and overlaps partly with seismic line GeoB00-142. The insert map in Fig. 3 also shows the location of the CSEM experiment that was installed at the Ocean Networks Canada (ONC) node at Bullseye vent. Analyses of CSEM data collected here indicate a resistivity of ∼5 Ωm in a ∼40-m thick overburden layer underlain by a less resistive half-space of ∼0.7 Ωm suggesting shallow gas hydrate and/or free gas occurrences (Mir 2011).

3 MARINE CSEM METHOD AND INSTRUMENTATION

Marine CSEM is a geophysical exploration method to investigate the electrical resistivity distribution of the subseafloor. The method is based on the propagation of electromagnetic fields through the subseafloor and seawater, which are generated by an electric or magnetic source dipole close to or on the seafloor. The signals recorded by one or more electric or magnetic receivers can be analysed to yield estimates of the subseafloor resistivity. The electrical resistivity of marine sediments is mainly controlled by the porosity and the pore fluid (typically conductive seawater). The presence of gas hydrate and free gas may increase the bulk resistivity where it replaces the pore fluid in the sediment matrix (e.g. Edwards *et al.* 2010). Marine CSEM measurements presented here were carried

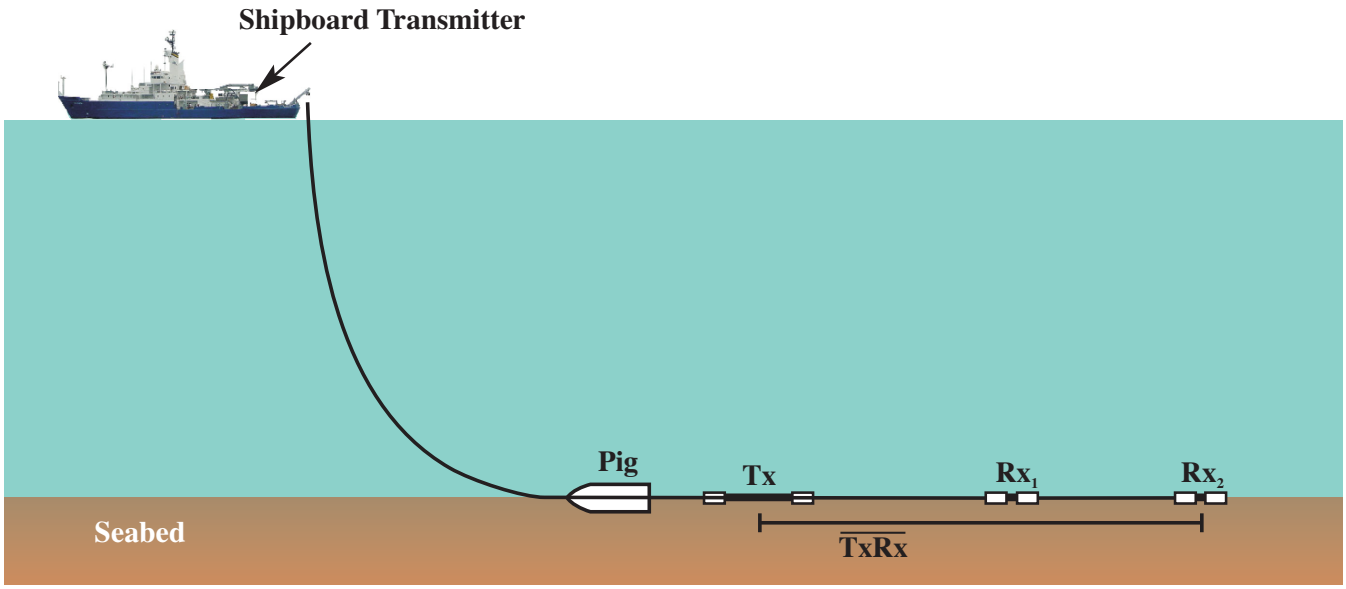

Figure 4. Configuration of the seafloor-towed horizontal dipole–dipole CSEM instrument with transmitter (Tx)–receiver (Rx) spacing $\overline{\text{TxRx}}$ (Schwalenberg *et al.* 2005; Yuan & Edwards 2000). Figure not to scale.

out with the time-domain electrical dipole-dipole system shown in Fig. 4. The system was developed at the University of Toronto for the investigation of marine gas hydrates (Edwards 1997; Yuan & Edwards 2000). When deployed on the seafloor the system consists of a 123-m long electrical transmitter dipole (Tx) followed by two 14-m long electrical receiving dipoles at offsets of 174 m and 292 m from the Tx measuring the inline-component of the ambient electrical fields with a pair of silver/silver chloride electrodes. A heavy, plough-shaped weight, called a 'pig', is attached to the front end of the array to keep it on the seafloor. The array is connected to the research vessel with a coaxial tow cable, and the receiver units and dipoles are connected to the Tx unit with simple rope of sufficient tensile strength. The current signal is a square waveform with a period of 6.6 s and a peak-to-peak amplitude of 20 A at maximum which is generated by a custom-made current transverter situated on board the research vessel. The current signal is sent to the transmitter dipole on the seafloor via the coaxial tow cable. The autonomous seafloor receiver units (Rx) are each equipped with a data logger, a high-precision clock, analog electronics and batteries inside aluminum pressure cylinders. An identical unit was used on the ship to record the source current signal. CSEM data are collected by aligning the CSEM system on the seafloor where it is towed along lines making stops to record data at a series of way points (WP). Due to limited data storage at the time of the experiments, data processing was carried out in two steps. The first processing step was carried out during data recording. The raw analog time series recorded with both receiver units and the unit recording the source current were band-pass filtered to remove high-frequency noise and low-frequency electrode drifts, stacked during recording and stored in equal-length data sets. The second processing step was carried out after the experiment. The step-on response and its standard deviation, which are used as input in the inversion described in Section 4, were obtained when stacking periodic half periods recorded at each WP. Fig. 5 shows a set of step-on responses and source signals (inset) measured on August 11th 2005. The data are generally of moderate quality. Differences in the electrical field responses may indicate variations in the seafloor resistivity along the profile, for example, earlier arrival and higher amplitude of the step-on response are related to a higher resistivity in the subsurface. Table 1 gives an overview of the survey lines analysed in this study.

4 INVERSION METHODS

Inversion methods can be applied to estimate a model of the subseafloor resistivity structure from observed CSEM data. Commonly, linearized inversion methods have been applied to CSEM data, which move down the data misfit gradient from an initial model and converge to a global or local minimum. Linearized inversion methods commonly use regularization to stabilize the inversion in case of ill-conditioned and singular problems. When carrying out multilayer inversions, a fundamental issue is that the amount of vertical structure resolved by the data is not known *a priori*. The most widely used linearized inversion method for CSEM is Occam's inversion (Constable *et al.* 1987) that aims for a minimum structure solution. When applied to a multilayer problem the model is intentionally overparametrized, but constrained by minimizing an L_2-norm of the second depth-derivative of the model resistivity. However, linearized inversion algorithms utilizing regularization are not well suited to quantitatively estimate model uncertainties.

This study addresses the question how much vertical structure can be resolved with the CSEM data assuming a 1-D model at each way point, and aims for a rigorous uncertainty estimation for the chosen parametrization. The overall choice of model, in this case a 1-D layered (blocky) model requires deliberate consideration of how the expected geological structure (inferred from, e.g. logging or seismic data) may be linked to the distribution of the geophysical parameter of interest (here, electrical resistivity). While blocky models are a common parametrization in geophysical inverse problems, the resistivity could also vary continuously with depth in gradients (e.g. due to compaction), and the choice of model type (blocky vs. gradient) could affect the number of layers required. For example, Steininger *et al.* (2014) used polynomial-spline models in seabed geoacoustic inversion to represent general gradients. However, gradient models can have difficulty matching abrupt structural changes. For the inversions in this paper, we adopted layered models to represent the relatively sharp resistivity contrast expected for gas

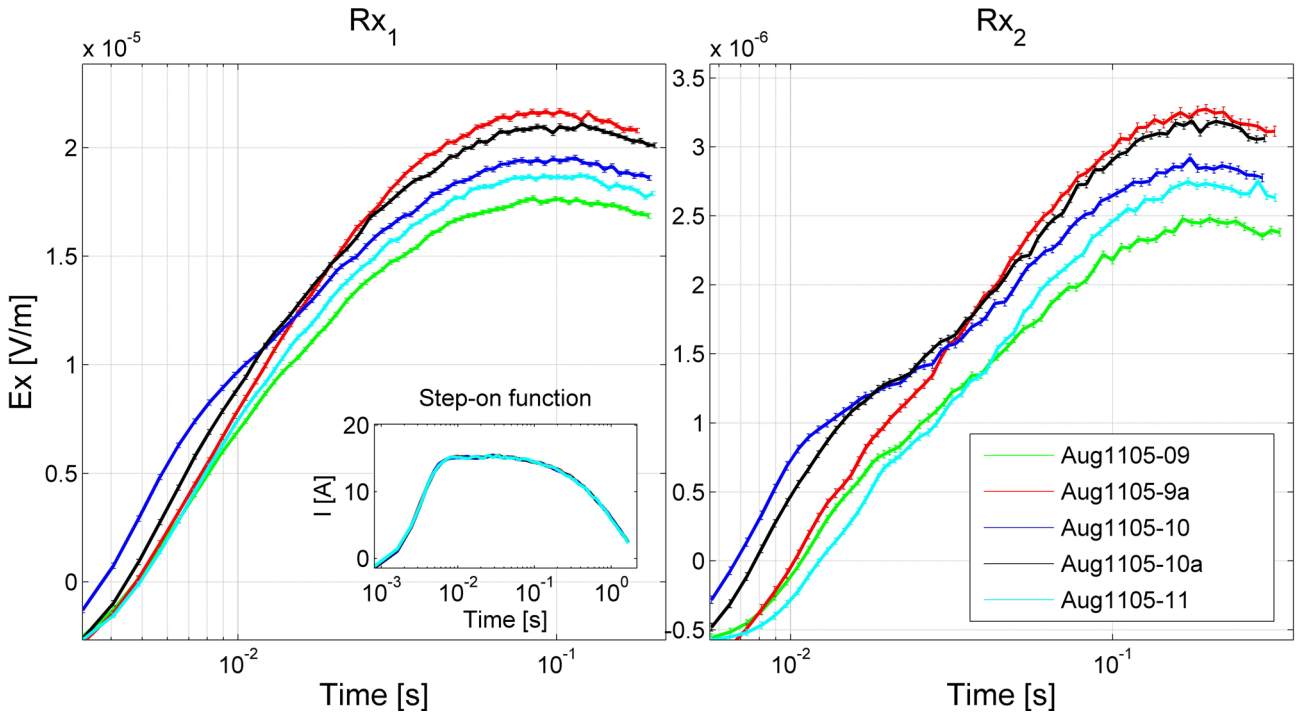

Figure 5. Observed data at two receivers with error bars (stacking standard deviation) and source signal (step-on function) for five adjacent WPs (9-11) of CSEM line Aug1105. Although the source signal, which was measured on board, is constant, the variation in late-time amplitude measured at the receivers suggests that the actual current injected at the transmitter electrodes varied (for this profile only). However, the difference in arrival time suggests that the subsurface is more resistive at WPs 10 and 10a than at the neighbouring WPs.

Table 1. CSEM data from 2005 to 2006 that were analysed for this paper.

	Line	Date	Comments
Area 1	Aug1105	11 Aug. 2005	Parallel to slope Tx electrode corroded
	Aug1205	12 Aug. 2005	Perpendicular to slope only data for Rx_2
	Sep0806	8 Sept. 2006	Perpendicular to slope
	Sep0906	9 Sept. 2006	Perpendicular to slope (not inverted with Bayesian inversion)
Area 2	Jul3105	31 July 2005	Across Bullseye vent

hydrate accumulations and lithological changes to older and denser accretionary sediments.

As a first inversion step in this study a nonlinear hybrid optimization (adaptive simplex simulated annealing, ASSA, which is described in Section 4.2) is implemented. We use the optimal solutions from ASSA and the BIC to determine the optimal number of layers resolved by the data, and subsequently apply Metropolis–Hastings sampling (MHS, Hastings 1970) with parallel tempering (Dosso *et al.* 2012) for this number of layers to sample the PPD over the parameter space. Parallel tempering improves the efficiency of geophysical parameter sampling (see e.g. Sambridge *et al.* 2014), especially when addressing nonlinear and multimodal behaviour, and has shown to be effective for marine CSEM data inversion (Ray *et al.* 2013a). In this approach, the parameters are perturbed in principal-component space (Dosso & Dettmer 2011) to sample more efficiently. Principal components consist of uncorrelated parameter combinations. Perturbation in principal-component space is advantageous for CSEM inversion as combinations of model parameters can often be better resolved than model parameters individually (e.g. resistivity-thickness product, Edwards 1997).

The nonlinear, numerical approach allows additional experimental parameters to be included in the inversion. Marginalizing over these additional parameters includes the effect of their uncertainties in the total uncertainty of the resistivity model. A multiplicative calibration factor (CF) is also included which scales the predicted step-on response (Scholl 2005). Amplifiers and electrode calibration values are already incorporated in the processing. However, the CF is implemented here to compensate for possible errors of survey parameters such as array geometry and amplitude recordings of the source signal. Another unknown included in the inversion is a small time delay representing drift of the Tx/Rx oven-heated crystal clocks that were synchronized on board but found to have drifted by up to 3 ms after instrument recovery (after ∼12 hours).

4.1 Bayesian formulation

Bayesian inversion seeks a statistical description of the model parameters by treating them as random variables. The distribution of the model parameters is given by the PPD, which combines prior knowledge about the parameters and information from the observed data vector **d** (Gelman *et al.* 2000). Bayes' rule can be written as

$$P(\mathbf{m}|\mathbf{d}, H) = \frac{P(\mathbf{d}|\mathbf{m}, H)P(\mathbf{m}|H)}{P(\mathbf{d}|H)}, \quad (1)$$

where H is the model parametrization (here, depending on an unknown number of subseafloor layers). The left side of eq. (1) represents the PPD, $P(\mathbf{m}|\mathbf{d}, H)$. The term $P(\mathbf{d}|\mathbf{m}, H)$ is the conditional probability of the data given the model parameters and parametrization. However, for fixed observed data and a specific choice of parametrization we interpret this term as the likelihood of the model parameters $L(\mathbf{m})$. The likelihood function implemented in this paper assumes Gaussian distributed errors and is explained in Section 4.4.

The term $P(\mathbf{m}|H)$ is the prior density of the model parameters given H, independent from the observed data. We treat priors as uniformly distributed between physically realistic upper and lower bounds for each model parameter. Resistivities are inverted in $\log_{10}$-domain and prior bounds are $\log_{10}(0.2\ \Omega\text{m})$ and $\log_{10}(200\ \Omega\text{m})$. The choice of the prior bounds is consistent with observed resistivity values. At X311 Site U1328 (Expedition 311 Scientists 2006a) resistivity values are locally as low as $\sim$0.2 Ωm (probably due to rapid gas hydrate formation). Also, resistivity values observed at marine cold vent systems worldwide have not been shown to exceed $\sim$200 Ωm (e.g. Collett *et al.* 2008; Kim *et al.* 2011). The probability for the observed data $P(\mathbf{d}|H)$ is the Bayesian evidence and can be considered the likelihood of the parametrization H given the observed data. The evidence can be approximated with the BIC (e.g. Schwarz 1978), which is used in this study to estimate the number of layers that can be resolved by the data (see Section 4.2). Bayes' rule can then be simplified for a fixed model parametrization H and written as

$$P(\mathbf{m}|\mathbf{d}) \propto L(\mathbf{m})P(\mathbf{m}). \tag{2}$$

Since the PPD is a multidimensional distribution, it is generally interpreted in terms of properties representing parameter estimates, uncertainties and interrelationships. In this study, parameter uncertainties are expressed as marginal probability densities and credibility intervals. Parameter estimates are analysed in terms of the median estimate of the marginal probability density profile of resistivity over depth. Parameter inter-relationships are examined in terms of joint marginal densities (see e.g. Dosso *et al.* 2006).

4.2 Bayesian information criterion

The BIC is derived from Bayes' rule (1) and can be used to estimate the most appropriate number of model parameters (here, resistivities and thicknesses for subseafloor layers) that can be resolved by the data. The misfit $E(\hat{\mathbf{m}}) = -\ln L(\hat{\mathbf{m}})$ of the maximum-likelihood model estimate $\hat{\mathbf{m}}$ decreases when additional layers are added, but at some point the model becomes over parametrized with unconstrained structure which can be geologically meaningless (an artefact of fitting the noise on the data). The BIC balances the data misfit with a penalty term which increases linearly with the number of parameters:

$$\mathrm{BIC} = 2E(\hat{\mathbf{m}}) + M\ln(N), \tag{3}$$

where M is the number of parameters and N the number of data.

To compute the maximum-likelihood model for different parametrizations, the data misfit is minimized over the parameter space using a nonlinear optimization, ASSA. ASSA is a hybrid algorithm which adaptively combines components of the global search method of fast simulated annealing (SA) with local downhill simplex (DHS) optimization. The algorithm minimizes the data misfit over a large, nonlinear parameter space and perturbs model parameters with dominantly stochastic perturbations (for a wide search) at early stages of the optimization, and with dominantly gradient-based perturbations based on the DHS method (for efficiency) at later stages. At all stages perturbations are accepted probabilistically as in SA. ASSA is an efficient method for strongly nonlinear problems with multiple local minima, correlated parameters and a wide range of parameter sensitivities (Dosso *et al.* 2001).

4.3 Metropolis–Hastings sampling

Markov-Chain Monte Carlo (MCMC) methods are typically employed to sample the parameter space in a random walk that converges in the long-run to sample the PPD. Here, MHS is applied (Metropolis *et al.* 1953; Hastings 1970). In this process the parameters of the current model are perturbed from $\mathbf{m} \rightarrow \mathbf{m}'$ using a proposal density $Q(\mathbf{m}'|\mathbf{m})$, here, a Gaussian distribution about $\mathbf{m}$. The proposed model is accepted according to the Metropolis–Hastings criterion with probability

$$\alpha = \min\left[1, \frac{P(\mathbf{m}')}{P(\mathbf{m})}\left(\frac{L(\mathbf{m}')}{L(\mathbf{m})}\right)^{1/T}\frac{Q(\mathbf{m}|\mathbf{m}')}{Q(\mathbf{m}'|\mathbf{m})}\right], \tag{4}$$

where T is a relaxation term, taken to be unity for unbiased sampling, but non-unity for parallel tempering (described below). The proposed model is accepted if a random number $\xi < \alpha$, where $\xi \in [0, 1]$. For uniform bounded priors and a symmetric proposal density, $Q(\mathbf{m}'|\mathbf{m}) = Q(\mathbf{m}|\mathbf{m}')$, eq. (4) simplifies to the likelihood ratio that we evaluate in terms of the misfit

$$\alpha = \min[1, e^{-(E(\mathbf{m}')-E(\mathbf{m}))/T}]. \tag{5}$$

In this study, MHS initially draws from a proposal distribution based on the linearized approximation to the PPD at an optimal model derived earlier with ASSA. The covariance of the proposal distribution is updated with sampled values as the inversion proceeds (Dosso & Dettmer 2011).

To ensure wide and efficient sampling of the parameter space, including isolated regions (modes) of high probability in the PPD, parallel tempering is applied here. Parallel tempering runs a series of MCMC chains at an increasing sequence of sampling temperatures $T \geq 1$. In comparison, SA (as used in ASSA) reduces temperatures towards zero to narrow down to an optimal model estimate. Higher temperatures, on the other hand, result in the acceptance of suboptimal models to sample the parameters space more widely in the search of new misfit minima. In parallel tempering, the various chains interchange models probabilistically (again following the Metropolis–Hastings acceptance criterion). The chain(s) sampled at $T = 1$ provide unbiased sampling of the PPD. However, interchange with higher-temperature chains provides efficient wide sampling (Earl & Deem 2005; Dosso *et al.* 2012; Sambridge 2014).

4.4 Likelihood

In this study, the likelihood function is based on the assumption that the data errors are zero-mean and Gaussian distributed with data covariance matrix $\mathbf{C}_d$, which is estimated from the data. These assumptions are verified *a posteriori* by applying statistical tests (Dosso *et al.* 2006). The joint likelihood function for a number of independent data sets with different covariance matrices (in this study, data sets for each receiver), becomes

$$L(\mathbf{m}, \mathbf{C}_{d_i}, a_i, i = 1, N_{\mathrm{Rx}}) = \prod_{i=1}^{N_{\mathrm{Rx}}}\left\{\frac{1}{(2\pi)^{N_i/2}\left|\mathbf{C}_{d_i}\right|^{1/2}} \cdot \exp\left[-\frac{1}{2}(\mathbf{d}_i - a_i\mathbf{d}_i(\mathbf{m}))^T\mathbf{C}_{d_i}^{-1}(\mathbf{d}_i - a_i\mathbf{d}_i(\mathbf{m}))\right]\right\}, \tag{6}$$

where N_{Rx} is the number of receivers, ^{T} indicates transpose, N_i is the number of data for the ith receiver, a_i is the CF for the ith receiver and $\mathbf{d}_i(\mathbf{m})$ are the predicted data for the ith receiver given model parameters $\mathbf{m}$ and a physical theory for the forward problem. The CF parameters are sampled implicitly within the inversion by

maximizing the likelihood with respect to a_i (for readability the i will be dropped in the following). Setting $\partial L(\mathbf{m}, \mathbf{C}_d, a)/\partial a = 0$ leads to

$$a = \frac{\mathbf{d}^T \mathbf{C}_d^{-1} \mathbf{d}(\mathbf{m})}{\mathbf{d}^T(\mathbf{m}) \mathbf{C}_d^{-1} \mathbf{d}(\mathbf{m})}, \tag{7}$$

which provides a closed form expression for the maximum-likelihood a estimate in terms of the model parameters $\mathbf{m}$ which are sampled explicitly (Dosso *et al.* 2006).

The inversion approach estimates both the optimal number of layers, using the BIC, and the data covariance matrices from residual analysis. An issue here is that the BIC requires an estimate of the data covariance matrix, while estimating this data covariance matrix requires knowledge of the number of layers (which is estimated using the BIC). Therefore, the approach applied here cycles twice through a set of inversions.

The first inversion with ASSA implements the standard deviations of the mean obtained from stacking the half periods of recorded CSEM data sets at each WP. The data covariance matrices $\mathbf{C}_{d_i}$ consist of variable variances (squared standard deviations) along the main diagonal and zero covariances. However, standard deviations from stacking represent data measurement errors (including electronic and ambient noise), which make up only one part of the data misfit in the inversion. Standard deviations from stacking do not represent theory errors due to model assumptions (e.g. 1-D parametrization), approximations in the physical theory and other uncertainties such as in the CSEM array geometry. Theory errors can dominate measurement errors and are often correlated. Here, as a first step, a scale factor δ_i^2 is included as an unknown that multiplies $\mathbf{C}_{d_i}$ of the ith receiver to account for larger errors (correlated errors are addressed in the second inversion cycle). This factor is inverted implicitly with ASSA by maximizing the likelihood with respect to δ_i^2 (setting $\partial L/\partial \delta_i^2 = 0$), where L is rewritten as

$$L(\mathbf{m}, \mathbf{C}_{d_i}, a_i, \delta_i^2, i = 1, N_{\mathrm{Rx}}) = \frac{1}{\prod_{i=1}^{N_{\mathrm{Rx}}} (2\pi)^{N_i/2}}$$
$$\cdot \exp\left[-\frac{1}{2} \sum_{i=1}^{N_{\mathrm{Rx}}} \left\{ (\mathbf{d}_i - a_i \mathbf{d}_i(\mathbf{m}))^T (\delta_i^2 \mathbf{C}_{d_i})^{-1} (\mathbf{d}_i - a_i \mathbf{d}_i(\mathbf{m})) \right\} \right.$$
$$\left. -\frac{1}{2} \sum_{i=1}^{N_{\mathrm{Rx}}} \left\{ \ln \left| \delta_i^2 \mathbf{C}_{d_i} \right| \right\} \right], \tag{8}$$

leading to (i is dropped for readability)

$$\delta^2 = \frac{1}{N} \left(\mathbf{d}^T \mathbf{C}_d^{-1} \mathbf{d} - \frac{(\mathbf{d}^T \mathbf{C}_d^{-1} \mathbf{d}(\mathbf{m}))^2}{\mathbf{d}^T(\mathbf{m}) \mathbf{C}_d^{-1} \mathbf{d}(\mathbf{m})} \right), \tag{9}$$

which is substituted back into eq. (8). ASSA is applied for three models with 1 to 3 layers. The model with the smallest BIC value is selected as the model with the optimal number of layers. The residual errors for this optimal model estimate $\hat{\mathbf{m}}$, defined as

$$\mathbf{r}_i = \mathbf{d}_i - a_i \mathbf{d}_i(\hat{\mathbf{m}}), \tag{10}$$

are considered one realization of the underlying error process (representing measurement and theory errors). Variances from the stacking process are not constant along the main diagonal (e.g. standard deviations from stacking have been shown to be higher when the electric fields are close to zero), and error correlations are especially large for early, closely spaced data samples, but decline quickly. While we consider correlation over time, Ray *et al.* (2013b) only used a small number of frequencies, but a denser grid of transmitter and receiver spacings, and considered spatial correlation instead. To account for correlated errors over time, we estimate a non-diagonally constant (non-Toeplitz) matrix from residual errors. As a first step, residual errors are standardized by their estimated standard deviation to $\tilde{\mathbf{r}}_i = \mathbf{r}_i / \hat{\boldsymbol{\sigma}}_i$ with (i is dropped for readability)

$$\hat{\sigma}_j^2 = \frac{1}{n} \sum_{l=j-n/2}^{j+n/2} r_l^2 \tag{11}$$

for a window of data samples of width n centred at the current data point j to accommodate standard deviations which vary slowly across the data set. The non-Toeplitz data covariance matrix is estimated by computing the autocorrelation of the residuals for each receiver, analogously to Dosso *et al.* (2006), with (i is dropped for readability)

$$\hat{C}_{d\,jl} = \frac{1}{N} \sum_{k=1}^{N-|j-l|} (\tilde{r}_k - \bar{\tilde{\mathbf{r}}})(\tilde{r}_{k+|j-l|} - \bar{\tilde{\mathbf{r}}}) \cos^p \frac{\pi |j-l|}{2(N-1)}, \tag{12}$$

where $j = 1, N$, $l = 1, N$, $\bar{\tilde{\mathbf{r}}}$ is the mean of the standardized residuals, and $\cos^p \frac{\pi |j-l|}{2(N-1)}$ is a damping function which drops off more sharply for higher p values (here, $p = 16$). Damping is applied to suppress correlation values for widely spaced data samples as these covariances are expected to be small, and the available number of samples ($N - |j - l|$) may be insufficient to meaningfully estimate the covariance values. Correlated errors can also be addressed using an hierarchical scheme based on sampling over first-order autoregressive parameters as additional unknowns (see e.g. Dettmer *et al.* 2012; Steininger *et al.* 2013). However, additional inversion parameters may not be constrained by the data and introduce spurious structure, and fixed data covariance matrices were found to produce more stable inversion results in this work. Further, first-order autoregressive processes are not as general as the non-Toeplitz covariance matrices.

The updated non-Toeplitz covariance matrix is implemented into ASSA for a second inversion cycle. The final estimate for the most probable number of layers is determined by minimizing the BIC. MHS is then carried out starting at the optimal model after the second inversion with ASSA and BIC, and uses the non-Toeplitz covariance matrix (Dosso *et al.* 2006) to calculate the misfit with eq. (6). Standardized residuals are estimated and examined for the median model estimate of the resulting PPD by $\tilde{\mathbf{r}} = \mathbf{C}_d^{-1/2}(\mathbf{d} - a\mathbf{d}(\mathbf{m}))$, where $\mathbf{C}_d^{-1/2}$ is the Cholesky decomposition of $\mathbf{C}_d^{-1}$. The inversion procedure is illustrated in Fig. 6.

5 INVERSION RESULTS AND DISCUSSION

5.1 Number of subseafloor layers

As mentioned previously, the optimal number of subseafloor layers is estimated by minimizing the BIC, which requires minimizing the data misfit for different numbers of layers using ASSA. A representative example of this procedure is given in Fig. 7 for WP 11 from CSEM line Aug1105 where two layers are resolved. The number of layers that can be resolved generally varies between WPs and between CSEM lines. Over 50 per cent of the WPs are interpreted with half-space (1-layer) models, while about 40 per cent of the WPs can be represented by 2-layer models according to the information in the data, and the remaining ~10 per cent are made up of 3-layer models. The relatively small number of layers is due to the lack of resolution inherent to diffusion methods, the lack of strong resistivity contrast in the shallow penetration

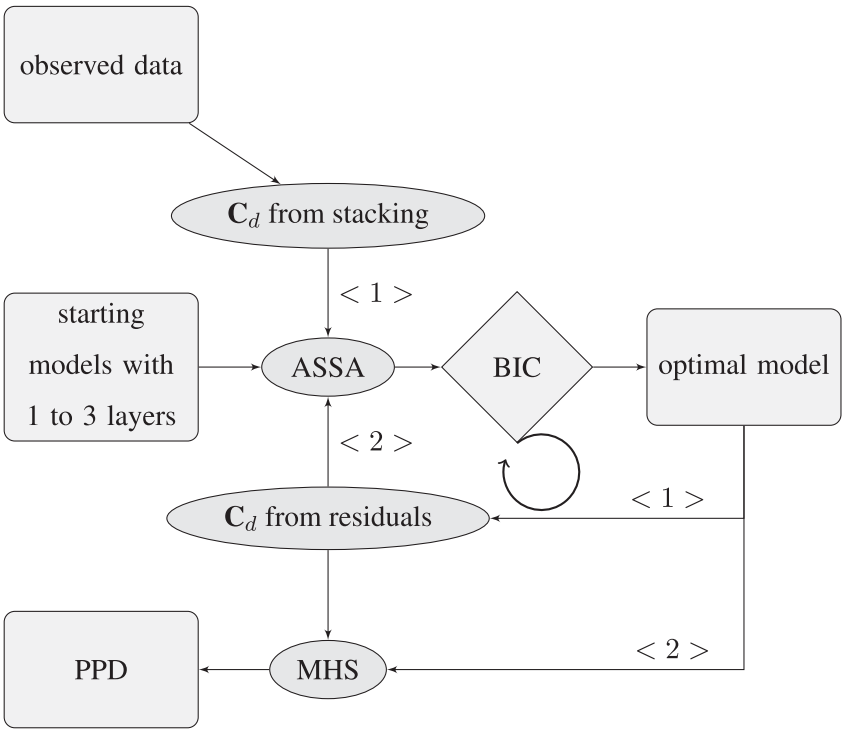

Figure 6. Inversion flow: < 1 > ASSA inversion for three models with 1 to 3 subsurface layers and a diagonal data covariance matrix from data stacking. Number of subsurface layers that can be resolved with the data is selected with BIC. A full non-Toeplitz data covariance matrix is estimated from residual error analysis. < 2 > ASSA inversion for three models with 1 to 3 subsurface layers and non-Toeplitz data covariance matrices. Number of subsurface layers that can be resolved with the data is selected with BIC. MHS samples the parameter space for this number of layers to obtain the PPD.

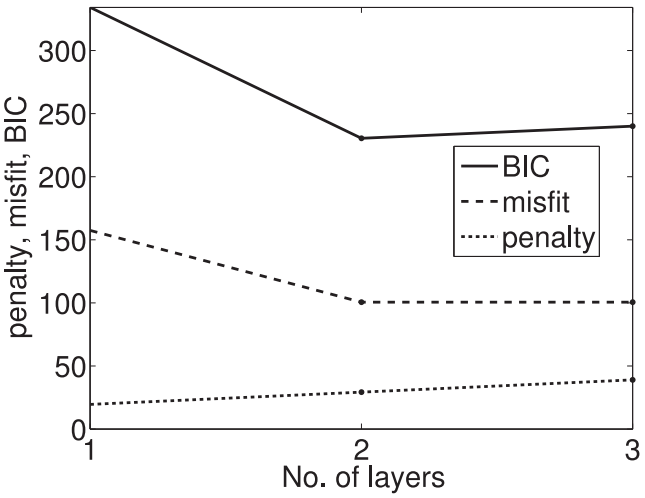

Figure 7. Bayesian information criterion (BIC) to evaluate the number of layers that are resolved with the data for WP 11 from line Aug1105. Here, two layers are resolved.

depth of the CSEM array (to ∼200 m depth), and the relatively low signal-to-noise ratio of the CSEM system used in these surveys (compared to more recently developed systems by Schwalenberg & Engels 2012).

5.2 Marginal probability profiles

After the number of layers is determined, MHS is applied to sample the parameter space. We demonstrate the characteristics of the resulting PPD of WP 11 from line Aug1105 at X311 Site U1329. The sampled PPD is shown in Fig. 8 in the form of marginal probability densities (bottom), joint-marginal probability densities (middle) for resistivities ρ, thicknesses *th*, calibration factors *a* and time delays *dt*, and a marginal probability density profile (top right) that represents the PPD as a function of depth and resistivity. Marginal probability densities represent uncertainty distributions for individual parameters, while joint marginals indicate relationships between parameters. Parameter relationships show some nonlinear behaviour, and parameters are both positively and negatively correlated. Taking into account parameter relationships may improve the interpretation, as, for example, done by Ray *et al.* (2014) who evaluate the resistivity–thickness (RT) product at gas-reservoir depth. While resistivities from inversion alone are generally underestimated compared to drill-hole resistivities, the RT product yields better agreement and can be converted to resistivities with seismic depth constraints. Joint marginals yield RT relationships other than the RT product, as, for example, illustrated by Minsley (2011) and in our work in Fig. 8. For instance, ρ_2 increases as th_1 increases, indicating the data are sensitive to a resistivity increase with depth, but cannot resolve the depth or the resistivity individually. Critical are the relationships between additional parameters such as the calibration factor *a* and time delay *dt* to the subseafloor parameters, which increase ambiguity and model uncertainty. For instance, ρ_1 is negatively correlated with dt_1 and dt_2; hence, not knowing the time delays exactly increases the uncertainty for ρ_1. On the other hand, knowing dt_1 better would reduce bimodality and constrain th_1 and ρ_2.

Parameter uncertainties are quantified with 95 per cent-credibility intervals (CI), which represent the narrowest interval containing 95 per cent of all model samples. Credibility intervals are shown as dashed black lines in all panels of Fig. 8. In the bottom panels it

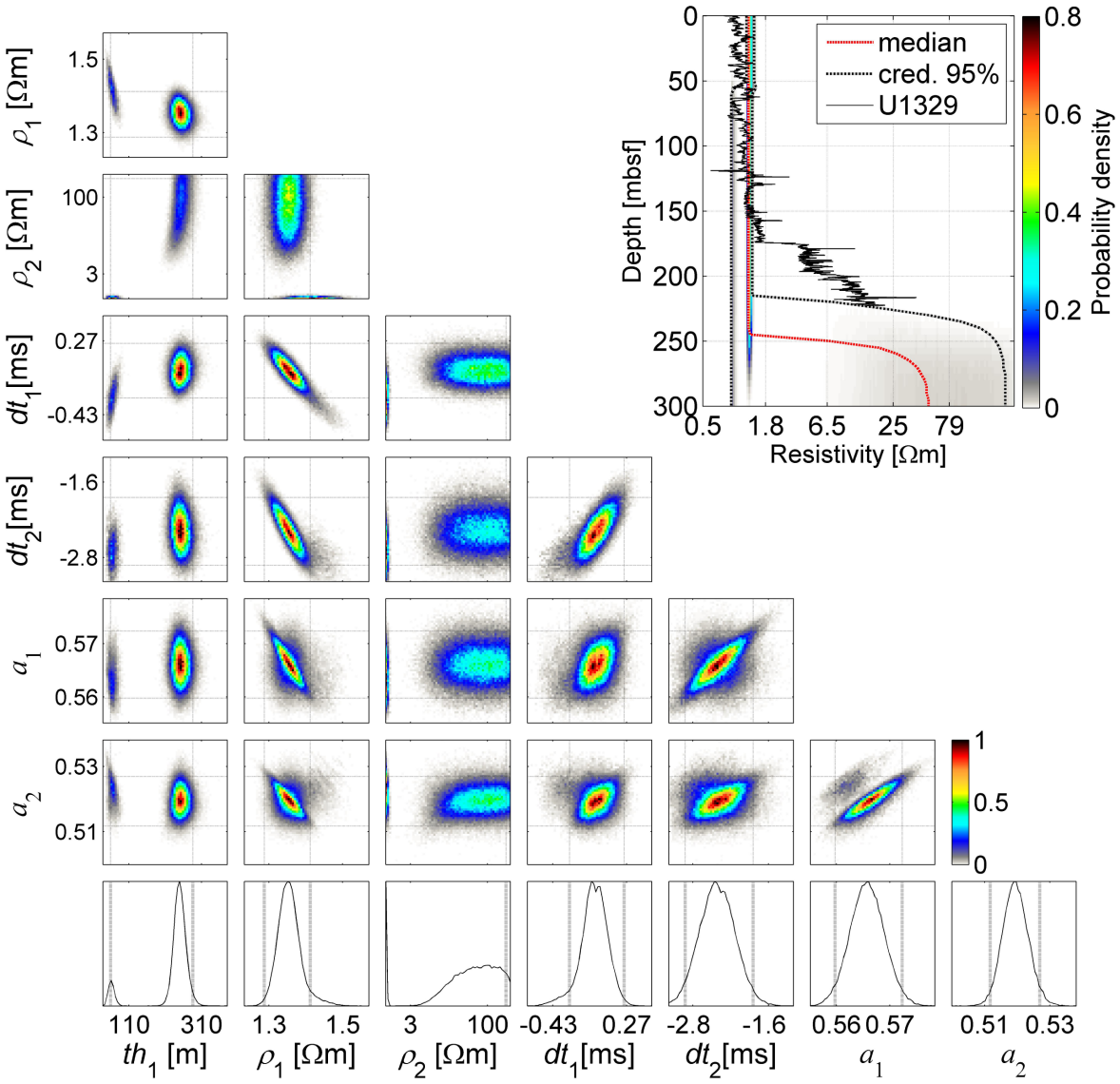

Figure 8. Inversion results for WP 11 from line Aug1105 in Area 1 close to X311 Site U1329. Bottom: marginal probability densities for each parameter (thickness th_l and resistivity ρ_l for the lth layer, as well as calibration factor a_i and time delay dt_i for the ith receiver). Middle: joint marginal probability densities (normalized to unit maximum) showing relationships between parameters. Top right corner: marginal probability density profile with posterior median model estimate and deep button average resistivities from U1329A. In all panels, dotted lines indicate 95 per cent credibility intervals.

can be observed that the CIs for ρ_1 are by two orders of magnitudes smaller than for ρ_2 as the resolution of the data is limited at greater depths. The probability density as a function of depth for WP 11 indicates an increase in resistivity between 220 to 250 mbsf. Within the first 150 m depth the inversion results match well with the measured LWD-resistivity (deep button average) at X311 Site U1329. The LWD measurements show an increase in resistivity starting at about 175 m depth due to the lower porosity of lithological Unit 3. However, this depth is not well resolved in the CSEM inversion results. The width of the CIs for the 2-layer model may underestimate the actual range of resistivities in the subseafloor, because we do not include uncertainty on the number of layers. Recent studies which include the number of layers as an unknown in the inversion (trans-dimensional CSEM inversion, Ray & Key 2012; Gehrmann *et al.* 2015) show uncertainties that generally increase quickly with depth.

Residual errors are calculated from predicted data of a 2-layer model that is similar to the posterior median model (red line, top right panel in Fig. 8) and has a high likelihood. Observed and predicted data for both receivers as well as standardized residuals are shown in Fig. 9. The standardized residual errors are examined with statistical tests (Dosso *et al.* 2006) for Gaussianity (Kolmogorov–Smirnov test, Massey 1951) and randomness (runs test). Standardized residual errors pass statistical tests if resulting p-values are larger than a significance level of 0.025, which is generally the case here. Histograms for standardized residuals at WP 11 compared to a standard Gaussian are shown in the bottom row of Fig. 9.

5.3 Area 1: inversion results and implications

Three CSEM lines around X311 Site U1329 were inverted with the Bayesian algorithm. Line Aug1105 (Fig. 10) along MCS line 89-08 is perpendicular to line Aug1205 (Fig. 11) along SCS line CAS05C-3, and perpendicular to line Sep0806 (Fig. 13) which intersects with line Aug1105 on the upper slope (see Fig. 2). Median posterior models for each WP (locations merged with the seismic

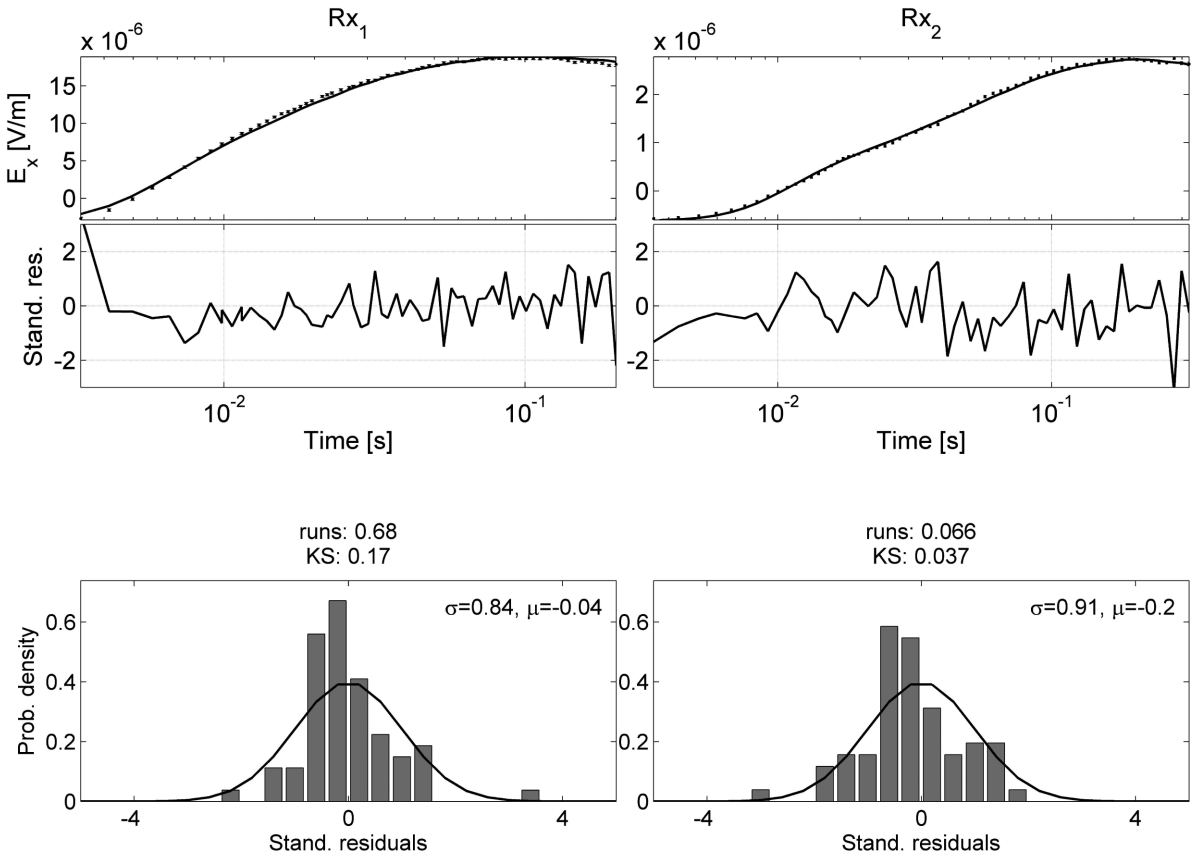

Figure 9. Top: step-on response for WP 11 from Aug1105 with observed data with standard deviations from $\mathbf{C}_d$ (crosses with error bars) and predicted data (black line) and standardized residuals. Bottom: histograms of standardized residuals compared to a standard Gaussian distribution with p-values for runs and KS test (title) and their standard deviation σ and mean μ (legend).

lines) are plotted in Figs 10 and 11 (upper panel) as coloured bars to represent the resistivity values. The bar widths correspond to the Tx-Rx$_2$ offset. The coloured bars overlap where WPs are close (generally ∼500 m apart with exception of the central part around X311 Site U1329 where they are ∼250 m apart). At each WP the credibility intervals are plotted as black lines which horizontal position represents the width of the credibility interval as a fraction of the prior resistivity bound width ($\log_{10}(200) - \log_{10}(0.2)$). We have chosen to show median models because they generally represent high probability regions of the marginal probability profiles. However, the reader is referred to Fig. 8 where the uncertainty information is displayed in terms of the marginal probability density profile, as well as marginal and joint marginal probability densities. More detailed display options have been used to image the PPD for 2-D profiles, for example, by Ray *et al.* (2014). Additional inversion parameters, shown in the bottom panels of Figs 10 and 11, are calibration factor a and time delay dt.

Line Aug1105: Fig. 10 shows results for CSEM line Aug1105 along MCS line 89-08. The seismic data (middle panel) acquired in 1989 show parallel layering of marine sediments representing Units 1 and 2 laying on top of highly disturbed, accreted sediments with a rugged surface (Unit 3). A BSR is observed on the middle slope (blue dashed line) as far landward as Site U1329, but cannot be observed further upslope. The base of the GHSZ is calculated from the observed BSR depths and extrapolated landward of U1329 following Gehrmann *et al.* (2009).

The Bayesian inversion reveals that a uniform resistivity distribution or half-space interpretation is adequate to explain the data at most of the measurement sites given the limited penetration depth of the array geometry (a fraction of the maximum offset, 292 m). Exceptions on line Aug1105 are WP 16 (possible venting site) and WPs 7a to 14, where 2 layers with a deep-situated resistive layer are more probable. This layer may relate to the sediment unconformity seen on MCS line 89-08 (red dashed line, second panel in Fig. 10), which is characterized by a decrease in porosity and increase in resistivity, as seen in the borehole log data of X311 Site U1329. The deep-situated resistive layer has wide CIs, which reflects the penetration limit of the CSEM array. The same unconformity lies relatively close to the seafloor between WP −1 and 2, but only WP 1 resolves two layers with an elevated resistivity below ∼20 mbsf.

The very pronounced resistivity anomaly at WP 16 on line Aug1105 is located at the landward edge of the GHSZ. This might be related to gas hydrate or free gas accumulations. MCS line 89-08 reveals a normal fault that may support upward migrating fluids transporting gases. There are no indications (e.g. diffractions, seismic blanking) of gas hydrate or free gas in the seismic data at this location. However, several localized venting sites have been detected along the upper slope of the margin (Riedel *et al.* 2006b). The main frequencies of MCS line 89-08 were chosen to penetrate the deeper subsurface structure, and may not resolve the upper 100 m in detail. Small gas hydrate lenses or along-fault rising gases may be outside the resolution limits. The resistivity anomaly at WP 16 is localized but consistent: It was observed on two consecutive days (the profile was repeated due to technical reasons) and also on the perpendicular line Sep0906 (not shown) where it intersects with line Aug1105 (see Fig. 2).

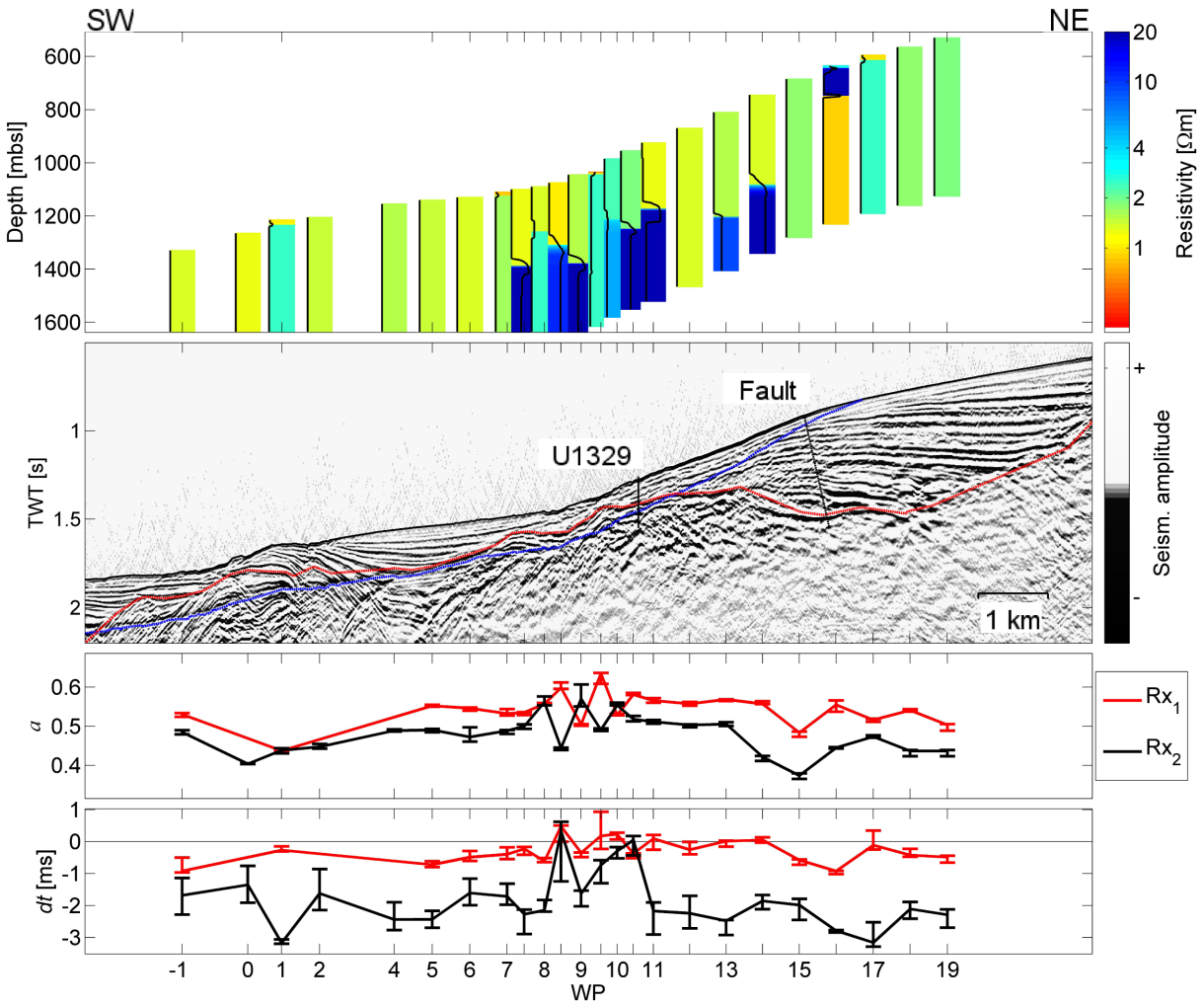

Figure 10. Top: CSEM median resistivity models for line Aug1105 with CI width (black line) normalized so that the maximum width equates to the width of the coloured bars. Middle: MCS line 89-08 with X311 Site U1329, observed and extrapolated BSR (blue dashed line) and sediment unconformity (red dashed line). Bottom: calibration factor (*a*) and time delay (*dt*) for each receiver, error bars represent 95 per cent CIs.

The CFs for both receivers are about half of the expected value 1, which might indicate that the current induced into the seafloor while acquiring CSEM line Aug1105 might have been about half of the value recorded with a Hall sensor on the ship. This could have been caused by a corroded connection at one transmitter electrode which was noticed and repaired after the deployment.

The inverted time delays, which correspond to a drift of the receiver and transmitter clocks after synchronization, are between 0 to −1 ms for Rx_1 and less consistent for Rx_2 with a mean value between −1 to −3 ms. The rugged trend likely relates to correlation between the subseafloor parameters and *dt*. However, the total drift measured on board after the instrument was recovered was −0.2 ms for Rx_1 and −1.2 ms for Rx_2, which fall within the inferred time delay range. We assume that most of the drift occurred due to temperature and pressure changes at the beginning and end of the deployment (when the instrument was lowered to or risen from the seafloor) rather than between WPs. Another reason for the erratic trend of the experiment parameters between WPs 8 and 11 could be the topographic change along the profile and perpendicular to it which we do not account for in the 1-D inversion.

Line Aug1205: CSEM line Aug1205 is perpendicular to line Aug1105 and coincident with SCS line CAS05C-3. Only the data sets of WPs 11 to 16a have been inverted with the Bayesian inversion, and the results are shown in Fig. 11. The seismic data (middle panel) show a strong BSR that might also coincide with the unconformity observed on MCS line 89-08. At WP 13 minor seismic blanking is observed, and the CSEM model indicates elevated resistivity which might be related to gas venting or gas hydrate accumulations. Other WPs have lower resistivities at shallow depths, but higher resistivities starting at ∼150 to 200 mbsf which might be related to resistive material of geological Unit 3. The inferred time delay for Rx_2 is between −1 and −2 ms.

The southeastern part of Aug1205, WP 3 to 11, has only been inverted with a linearized Marquardt inversion (Scholl 2010) for half-space resistivities due to the rough topography, and is shown in Fig. 12 on top of the 3.5-kHz sub-bottom profiler data. The pronounced resistivity anomaly at WP 6 is located on the edge of a shell-shaped topographic depression. The anomaly could be caused by free gas rising along a fault plane that might also have caused the depression to form during a slide event. If this is the case, this feature would be of interest for further studies of the stability of the upper slope. The 3.5-kHz sub-bottom (chirp) profiler data show elevated amplitudes and a reflector that might relate to an erosional surface that was refilled (black arrow in bottom panel of Fig. 12). The resistivity anomaly at WP 6 is significantly larger than others in this area, and is unlikely caused by topographic effects alone,

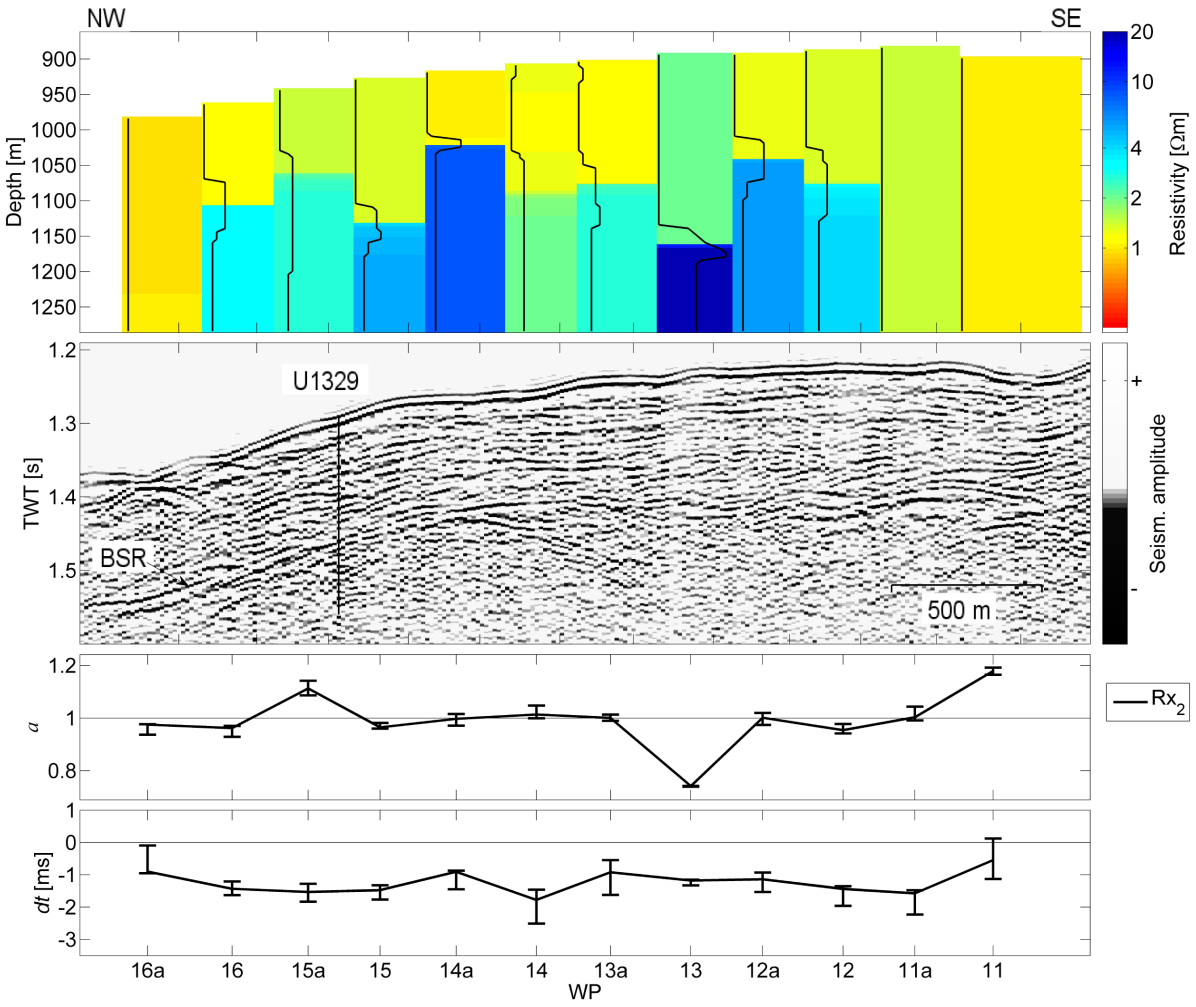

Figure 11. Top: CSEM median resistivity models with 95 per cent CI width (black lines) for line Aug1205. Middle: SCS line Cas05C-3 with Site U1329 (black line). Bottom: CF and time delay between Tx and Rx (error bars represent 95 per cent CIs).

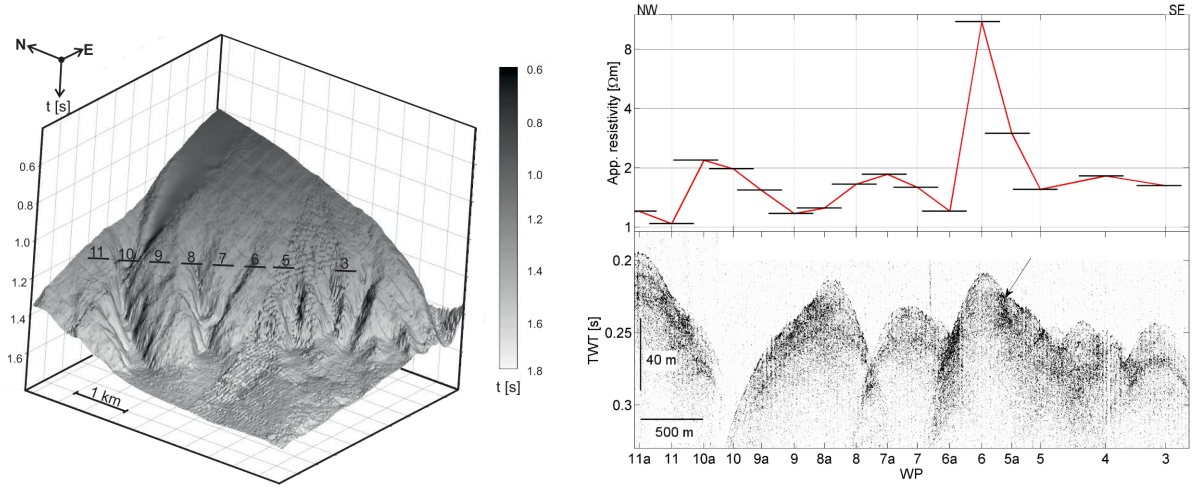

Figure 12. Left: bathymetry at the southeast end of line Aug1205 [in two-way-traveltime (s)]. Right, top: apparent resistivities for CSEM data at receiver 2, black solid lines represent the length of the instrument and position (assuming a flat seafloor). Right, bottom: 3.5-kHz sub-bottom profiler data, arrow pointing to erosional surface.

whereas elevated apparent resistivities between WP 7 and 11a are difficult to interpret due to the strong seafloor topography changes relative to the length of the CSEM array (which may introduce geometry errors not accounted for in the inversion).

Line Sep0806: Bayesian inversion results for line Sep0806 (see Fig. 13) reveal that at most WPs only a single layer is resolved with generally higher resistivities on the upper slope compared to resistivities down the slope on lines Aug1105 and Aug1205. The

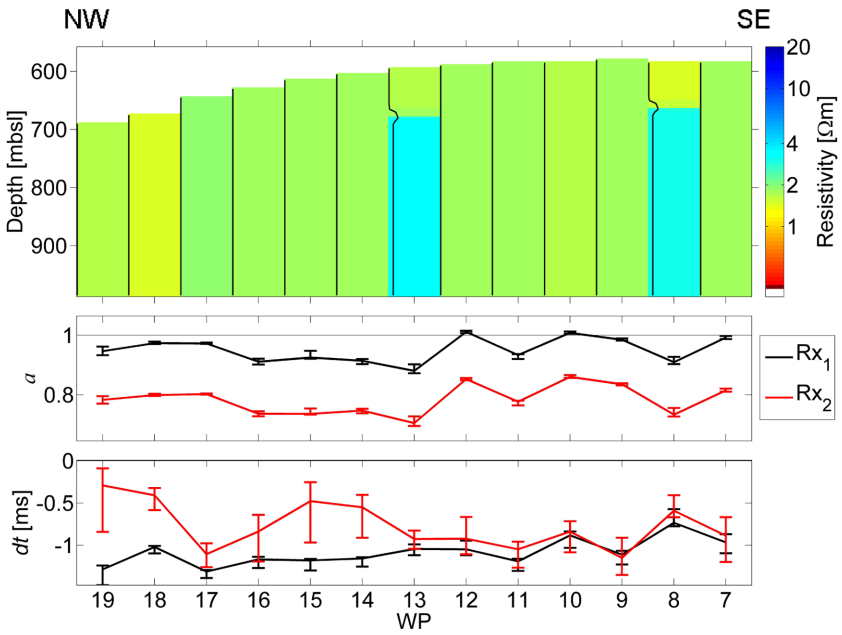

Figure 13. Top: median resistivity models with uncertainties (black lines) along line Sep0806. Bottom: calibration factor (a) and time delay (dt), error bars represent 95 per cent CIs.

mean values for the CF for Rx_1 are around 1, while mean values for Rx_2 are around 0.8. The inferred time delays are only about −1 ms for the data set collected in 2006.

5.4 Area 2: inversion results and implications

Line Jul3105: We analysed CSEM line Jul3105 in Area 2 in vicinity of X311 Site U1328 which crosses the Bullseye vent (see Fig. 3) with the Bayesian inversion. Resistivity median models are shown in Fig. 14 on top of MCS line GeoB00-142. The CSEM WPs are projected onto the seismic line with a maximum projection distance of 1 km at WP 1. The seismic section (middle panel on Fig. 14) shows several high amplitude reflections and seismic blanking at X311 Site U1328 which may relate to gas hydrates or free gas in the sediment. Sediment reflectors at U1328 are seemingly distorted, which might be caused by a shorter traveltime through sediments containing massive gas hydrates or by faulting. Seismic amplitudes increase west of Site U1328 at 1.92 to 1.98 s two-way traveltime (twt) close to the base of the GHSZ. Older, distorted, accretionary-wedge sediments are uplifted on both sides of U1328, and are overlain with younger, stratified slope deposits. Bullseye vent is the most dominant feature, centred on CSEM line Jul3105 at WPs 14 and 15 (see Fig. 3). Inversion results at WPs 13 and 14 reveal high resistivities around ∼25 Ωm within the first 70 to 100 mbsf, and lower resistivities around 1 Ωm below. At these WPs the lower bound for the second layer is set to 0.9 Ωm to avoid geologically unreasonable resistivities (likely introduced by 3-D effects). Observed gas plumes and bacterial mats (see Fig. 3) at the same location support the presence of shallow gas hydrate or free gas. Inversion results of WP 14 close to Site U1328 match with the high resistivities observed during drilling (see Fig. 15). We suggest that the high resistivities are caused by massive gas hydrates, which were found during piston coring (Riedel *et al.* 2006b). The inversion at WP 15 introduces a deeper resistive layer, which might relate to resistive material at greater depth. The seismic reflector on MCS line GeoB00-142, that may relate to a gas hydrate cap, is also deeper at WP 15 than at WP 14. However, we do not account for 3-D effects that are likely present at the vent site, and therefore need to interpret the inversion results here with caution. Uncertainties at greater depths are likely higher than illustrated. At WPs 18 and 25 resistivities of ∼2.5 Ωm within the upper 100–150 mbsf were inferred which may be related to the presence of free gas or gas hydrate underlain by a less resistive half-space. Comparing the vertical position of the elevated resistivities at WP 18 within the seismic section suggests that the higher resistivities are within the shallow, younger sediments, rather than in the older, accreted sediments. Additionally, sub-bottom profiler data obtained with an autonomous underwater vehicle (Paull *et al.* 2009) show seismic blank zones at WP 18 that may indicate the presence of fluid venting and/or gas hydrate occurrences.

At WP 9 an interval of ∼4 Ωm at depths of 90 to 200 mbsf is inferred that might be related to elevated seismic amplitudes and faults seen on the projected seismic reflection line GeoB00-142. Again, the possible explanation could be the presence of free gas or gas hydrate. The CF is around 1 which indicates only small deviations from the assumed geometry of the CSEM array, and other survey parameters. The time delay is between −1 and −2 ms for Rx_1 and between −3 and −4 ms for Rx_2.

6 CONCLUSIONS

Time-domain marine CSEM data were acquired in 2005 and 2006 in two survey areas on the middle and upper continental slope of the northern Cascadia margin in the vicinity of IODP Expedition 311 Sites U1328 and U1329. A seafloor-towed electric dipole-dipole system was used which records the inline electric field components at two receiver dipoles at offsets of 174 m and 292 m from the source dipole respectively. We used a 1-D nonlinear Bayesian inversion to estimate model parameters and uncertainties. Survey parameters, that is, time drift of the receiver clocks and a calibration factor, have been included as unknown parameters in the inversion. The BIC was applied to select the number of subsurface layers that can be resolved with the data, which was generally found to be one or two (sometimes three) layers. The parameters were sampled in principle-component space with MHS

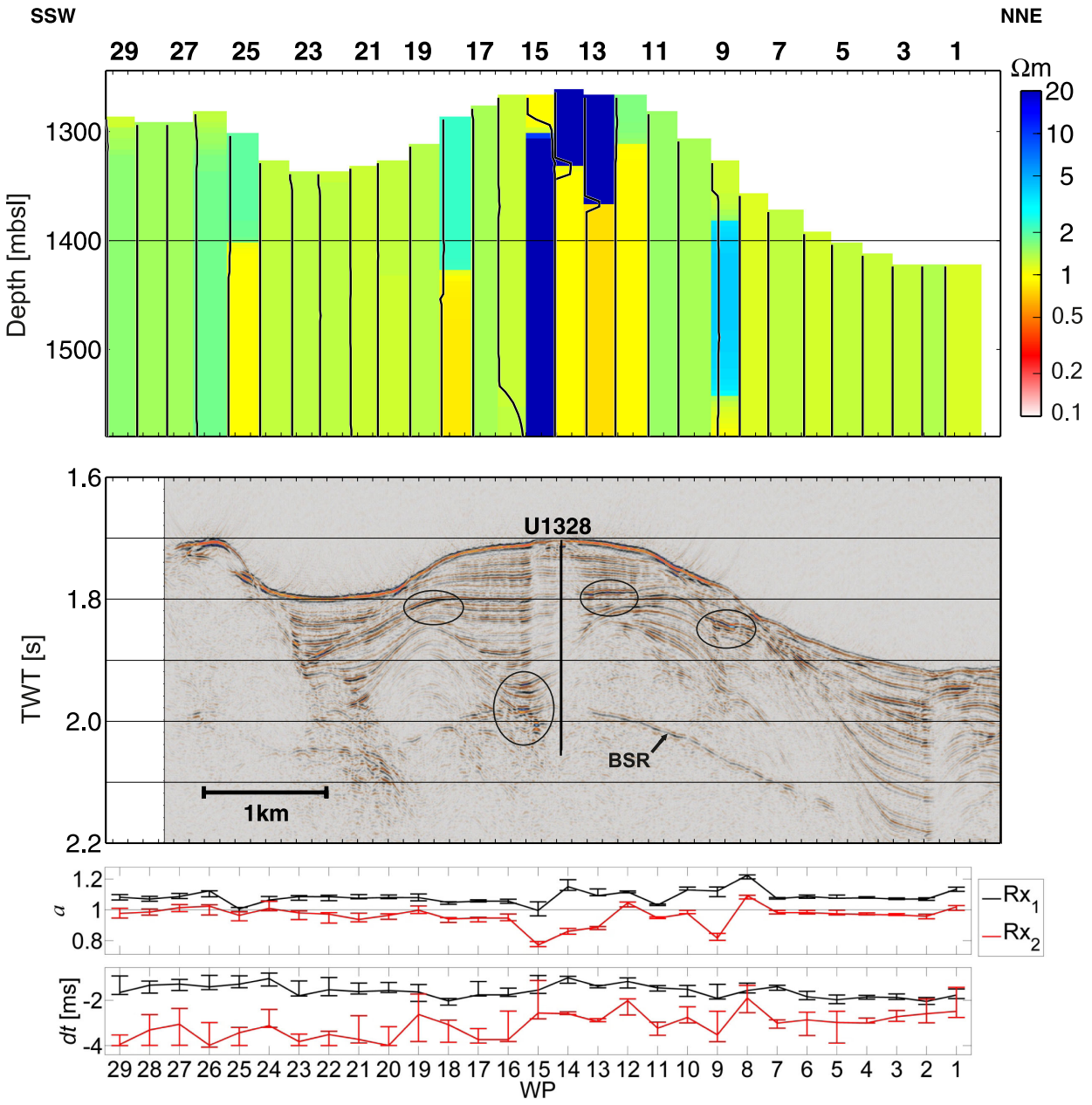

Figure 14. Top: median resistivity models with uncertainties (black lines) for line Jul3105. Middle: MCS line GeoB00-142 with X311 Site U1328. Bottom: calibration factor (a) and time delay (dt), error bars represent 95 per cent CIs.

and the resulting PPD contains information about model parameter uncertainties and relationships. Parameter uncertainties increase significantly for deeper structure, but might be generally underestimated due to the assumption that the number of subsurface layers is determined exactly. For example, LWD resistivities from drilling extend the inferred credibility interval for resistivities at greater depth (see Figs 8 and 15) but they generally match the inferred resistivity trend. Alternatively, the number of subsurface layers can be included within a trans-dimensional inversion such as implemented for marine CSEM data by Ray & Key (2012) and Gehrmann *et al.* (2015) to better estimate uncertainties (especially in greater depth). Trans-dimensional inversion has advantages in that it requires less user intervention and accounts for the uncertainty in the parametrization in the parameter uncertainty estimates. However, achieving convergence in trans-dimensional sampling can be more challenging than in fixed-dimensional inversions. The BIC-based approach for the smallest number of parameters that can be resolved by the data enables efficient and stable sampling in principal-component space with a relatively small number of forward computations.

The following geological interpretation can be drawn. A major resistivity contrast found by CSEM inversion is caused by a sediment unconformity around Site U1329. The sediment unconformity divides younger marine sediments from denser accreted sediments (∼5 Ma older). Resistivities of the deeper layer are higher and have wider credibility intervals ranging from ∼10 to 100 Ωm. On the upper slope, on the landward edge of the GHSZ, we infer three sites (WP 16 on line Aug1105 and WP 6 and 13 on line Aug1205) with anomalously high resistivities that might be caused by gas hydrate or free gas occurrences at possible cold vents (although neither gas

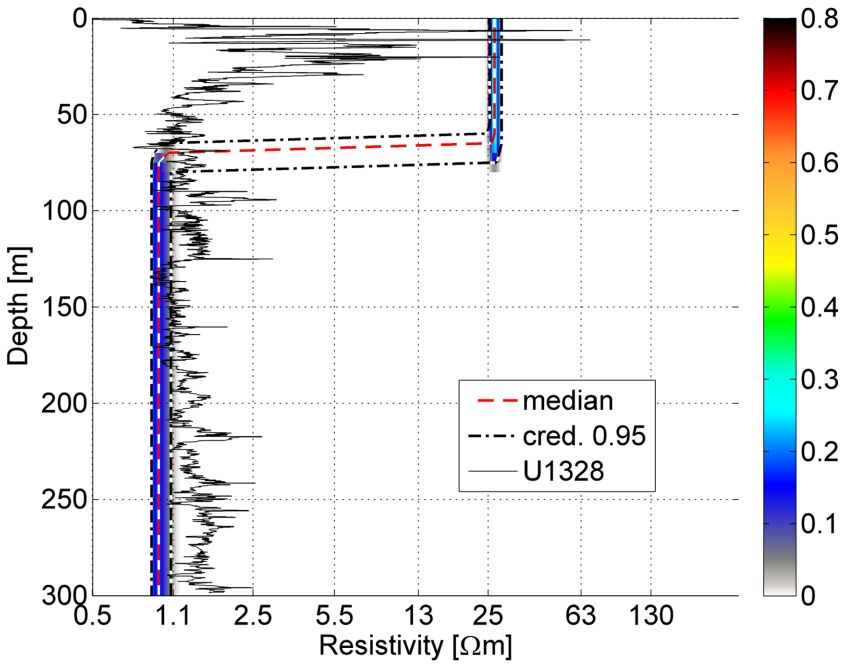

Figure 15. Marginal probability density profile with posterior median model estimate at WP 14 of Jul3105 and deep button average resistivities from U1328A.

hydrate nor gas plumes have been observed at these locations, yet). Generally elevated resistivity values on the upper slope along line Aug1105 are probably due to sediment erosion that exposes deeper, more compacted sediments. At Site U1328 on the middle slope of the margin, elevated subseafloor resistivity values (>20 Ωm) were inferred associated with massive gas hydrates at Bullseye vent. Additional gas venting sites on both flanks around the main vent also cause elevated resistivity values.

Overall, the 1-D nonlinear statistical inversion revealed that the data sets contain limited information on the vertical resistivity structure. We believe this is due to the lack of strong resistivity contrasts within the penetration depth of the instrument (maximum offset 292 m), the 1-D assumption in modelling vent structures which are likely 2-D or 3-D, the relatively low signal-to-noise ratio compared to recently developed instruments (Schwalenberg & Engels 2012), and erroneous (uncertain) survey parameters including array geometry, source current amplitude and clock drift. Joint marginal probability densities additionally reveal significant parameter correlations between unknown experiment parameters (such as calibration factor and time delay) and subseafloor parameters. However, the nonlinear Bayesian inversion defines a range for unknown acquisition parameters that agree with presumptions (e.g. observed clock drift after instrument recovery). The Bayesian inversion also reveals well constrained, one layer models with typical seafloor resistivities between 1 and 1.5 Ωm at most sites along the lines. Other sites, where the resistivity structure correlates with seismically inferred vent structures, seismic amplitude anomalies, and a sediment unconformity, are more likely to be explained with a two- (sometimes three-) layer resistivity model. Parameters and uncertainties agree at neighbouring way points and with local resistivity data from logging during the IODP Expedition 311.

ACKNOWLEDGEMENTS

We thank the Coast Guard crew of CCGS John P. Tully and scientific party of Prof R. Nigel Edwards from the University of Toronto for collecting the presented CSEM data in 2005 and 2006. We would also like to thank Carsten Scholl for the 1-D CSEM forward code. Finally, we would like to thank Rene-Edouard Plessix, Anandaroop Ray and an anonymous reviewer for their constructive comments.

REFERENCES

Buland, A. & Kolbjørnsen, O., 2012. Bayesian inversion of CSEM and magnetotelluric data, *Geophysics,* **77**(1), E33–E42.

Chen, J., Hoversten, G.M., Vasco, D., Rubin, Y. & Hou, Z., 2007. A Bayesian model for gas saturation estimation using marine seismic AVA and CSEM data, *Geophysics,* **72**(2), WA85–WA95.

Collett, T. *et al.*, 2008. Indian National Gas Hydrate Program (NGHP) Expedition 01, Initial Report.

Constable, S. & Srnka, L.J., 2007. An introduction to marine controlled-source electromagnetic methods for hydrocarbon exploration, *Geophysics,* **72**(2), WA3–WA12.

Constable, S.C., 2010. Ten years of marine CSEM for hydrocarbon exploration, *Geophysics,* **75**(5), 75A67–75A81.

Constable, S.C., Parker, R.L. & Constable, C.G., 1987. Occam's inversion: a practical algorithm for generating smooth models from electromagnetic sounding data, *Geophysics,* **52,** 289–300.

Dash, R. & Spence, G., 2011. P-wave and S-wave velocity structure of northern Cascadia margin gas hydrates, *Geophys. J. Int.,* **187**(3), 1–15.

Davis, E.E. & Hyndman, R.D., 1989. Accretion and recent deformation of sediments along the northern Cascadia subduction zone, *Geol. Soc. Am. Bull.,* **101,** 1465–1480.

Davis, E.E., Hyndman, R.D. & Villinger, H., 1990. Rates of fluid expulsion across the northern Cascadia accretionary prism: constraints from new heat flow and multichannel seismic reflection data, *J. geophys. Res.,* **95**(B6), 8869–8889.

Dettmer, J., Molnar, S., Steininger, G., Dosso, S.E. & Cassidy, J.F., 2012. Trans-dimensional inversion of microtremor array dispersion data with hierarchical autoregressive error models, *Geophys. J. Int.,* **188,** 719–734.

Dosso, S.E. & Dettmer, J., 2011. Bayesian matched-field geoacoustic inversion, *Inverse Problems,* **27**(5), 055009.

Dosso, S.E., Wilmut, M.J. & Lapinski, A.-L.S., 2001. An adaptive-hybrid algorithm for geoacoustic inversion, *IEEE Journal of Oceanic Engineering,* **26**(3), 324–336.

Dosso, S.E., Nielsen, P.L. & Wilmut, M.J., 2006. Data error covariance in matched-field geoacoustic inversion, *J. acoust. Soc. Am.,* **119**(1), 208–219.

Dosso, S.E., Holland, C.W. & Sambridge, M., 2012. Parallel tempering for strongly nonlinear geoacoustic inversion, *J. acoust. Soc. Am.,* **132**(5), 3030–3040.

Earl, D.J. & Deem, M.W., 2005. Parallel tempering: Theory, applications, and new perspectives, *Phys. Chem. Chem. Phys.,* **7,** 3910–3916.

Edwards, R.N., 1997. On the resource evaluation of marine gas hydrate deposits using sea-floor transient electric dipole-dipole methods, *Geophysics,* **62**(1), 63–74.

Edwards, R.N., Schwalenberg, K., Willoughby, E.C., Mir, R. & Scholl, C., 2010. Marine Controlled-source Electromagnetics and the Assessment of Seafloor Gas Hydrate, in *Geophysical Characterization of Gas Hydrates,* pp. 149–162, eds Riedel, M., Willoughby, E.C. & Chopra, S., Society of Exploration Geophysicists.

Ellingsrud, S., Eidesmo, T., Johansen, S., Sinha, M.C., MacGregor, L.M. & Constable, S., 2002. Remote sensing of hydrocarbon layers by seabed logging (SBL): results from a cruise offshore Angola, *Leading Edge,* **21**(10), 972–982.

Expedition 311 Scientists, 2005. Cascadia margin gas hydrates, In *IODP Prel. Rept.,* vol. 311, p. 104. Integrated Ocean Drilling Program Management International, Inc., Washington, DC.

Expedition 311 Scientists, 2006a. Site U1328, in Riedel, M., Collett, T., Malone, M. & the Expedition 311 Scientists, *Proceedings of the Integrated Ocean Drilling Program,* vol. 311, Integrated Ocean Drilling Program Management International, Inc., Washington, DC.

Expedition 311 Scientists, 2006b. Site U1329, in Riedel, M., Collett, T., Malone, M. & the Expedition 311 Scientists, *Proceedings of the Integrated Ocean Drilling Program,* vol. 311, Integrated Ocean Drilling Program Management International, Inc., Washington, DC.

Gehrmann, R.A.S., Müller, C., Schikowsky, P., Henke, T., Schnabel, M. & Bönnemann, C., 2009. Model-Based Identification of the Base of the Gas Hydrate Stability Zone in Multichannel Reflection Seismic Data, Offshore Costa Rica, *International Journal of Geophysics,* **2009,** 12.

Gehrmann, R.A.S., Dettmer, J., Schwalenberg, K., Engels, M., Özmaral, A. & Dosso, S.E., 2015. Trans-dimensional Bayesian inversion of controlled source electromagnetic data in the German North Sea, *Geophys. Prospect.,* **63**(6), 1314–1333.

Gelman, A., Carlin, J., Stern, H. & Rubin, D., 2000. *Bayesian Data Analysis,* 2nd edn, Chapman and Hall/CRC.

Goswami, B., Weitemeyer, K., Minshull, T., Sinha, M. & Westbrook, G., 2013. CSEM Survey of a Methane Vent Site, Offshore West Svalbard, *Fire in the Ice,* **13**(2), 12–18.

Gunning, J., Glinsky, M.E. & Hedditch, J., 2010. Resolution and uncertainty in 1D CSEM inversion: A Bayesian approach and open-source implementation, *Geophysics,* **75**(6), F151–F171.

Haacke, R.R., Westbrook, G.K. & Hyndman, R.D., 2007. Gas hydrate, fluid flow and free gas: formation of the bottom-simulating reflector, *Earth planet. Sci. Lett.,* **261,** 407–420.

Hastings, W.K., 1970. Monte Carlo sampling methods using Markov chains and their application, *Biometrika,* **57**(1), 97–109.

Hoversten, G.M., Cassassuce, G., Gasperikova, E., Newman, G.A., CHen, J., Rubein, Y., Hou, Z. & Vasco, D., 2006. Direct reservoir parameter estimation using joint inversion of marine seismic AVA and CSEM data, *Geophysics,* **71**(3), C1–C13.

Hyndman, R.D. & Spence, G.D., 1992. A Seismic Study of Methane Hydrate Marine Bottom Simulating Reflectors, *J. geophys. Res.,* **97**(B5), 6683–6698.

Hyndman, R.D., Wang, K., Yuan, T. & Spence, G.D., 1993. Tectonic Sediment Thickening, Fluid Expulsion, and the Therman Regime of Subduction Zone Accretionary Prisms: The Cascadia Margin off Vancouver Island, *J. geophys. Res.,* **98**(B12), 21 865–21 876.

Kim, G.Y., Yi, B.Y., Yoo, D.G., Ryu, B.J. & Riedel, M., 2011. Evidence of gas hydrate from downhole logging data in the Ulleung Basin, East Sea, *Marine and Petroleum Geology,* **28**(10), 1979–1985.

Malinverno, A., Kastner, M., Torres, M.E. & Wortmann, U.G., 2008. Gas hydrate occurrence from pore water chlorinity and downhole logs in a transect across the Cascadia margin (Integrated Ocean Drilling Program Expedition 311), *J. geophys. Res.,* **113**(B8), B08103, doi:10.1029/2008JB005702.

Massey, F.J., 1951. The Kolmogorov-Smirnov Test for Goodness of Fit, *J. Amer. Statist. Assoc.,* **46,** 68–78.

Metropolis, N., Rosenbluth, A., Rosenbluth, M. & Teller, A.E., 1953. Equation of state calculations by fast computing machines, *J. Chem. Phys.,* **21**(6), 1087–1092.

Minsley, B.J., 2011. A trans-dimensional Bayesian Markov chain Monte Carlo algorithm for model assessment using frequency-domain electromagnetic data, *Geophys. J. Int.,* **187**(1), 252–272.

Mir, R.A., 2011. Design and Deployment of a Controlled Source EM Instrument on the Neptune Observatory for Long-Term Monitoring of Methane Hydrate Deposits, *PhD thesis* at University of Toronto.

Nimblett, J. & Ruppel, C., 2003. Permeability evolution during the formation of gas hydrates in marine sediments, *J. geophys. Res.: Solid Earth,* **108**(B9), doi:10.1029/2001JB001650.

Paull, C.K., Ussler, W., Caress, W.D., Thomas, H., Lundstein, E., Riedel, M. & Lapham, L., 2009. Seafloor manifestations of gas venting and near seafloor gas hydrate occurences, *AGU, Fall Meeting Suppl., Abstract,* OS23B-05.

Ray, A. & Key, K., 2012. Bayesian inversion of marine CSEM data with a trans-dimensional self parametrizing algorithm, *Geophys. J. Int.,* **191,** 1135–1151.

Ray, A., Alumbaugh, D.L., Hoversten, G.M. & Key, K., 2013a. Robust and accelerated Bayesian inversion of marine controlled-source electromagnetic data using parallel tempering, *Geophysics,* **78**(6), E271–E280.

Ray, A., Key, K. & Bodin, T., 2013b. Hierarchical Bayesian inversion of marine CSEM data over the Scarborough gas field – a lesson in correlated noise, in *2013 SEG Annual Meeting,* Society of Exploration Geophysicists.

Ray, A., Key, K., Bodin, T., Myer, D. & Constable, S., 2014. Bayesian inversion of marine CSEM data from the Scarborough gas field using a transdimensional 2-D parametrization, *Geophys. J. Int.,* **199**(3), 1847–1860.

Riedel, M., Spence, G.D., Chapman, N.R. & Hyndman, R.D., 2002. Seismic investigation of a vent field associated with gas hydrates, offshore Vancouver Island, *J. geophys. Res.,* **107**(B9), EPM 5-1–EPM 5-16.

Riedel, M., Collett, T. & Malone, M., 2006a. Expedition 311 synthesis: scientific findings, in *Proceedings of the Integrated Ocean Drilling Program,* Vol. 311, pp. 1–28, eds Riedel, M., Collett, T., Malone, M. & the Expedition 311 Scientists, Integrated Ocean Drilling Program Management International, Inc., Washington, DC.

Riedel, M., Novosel, I., Spence, G.D., Hyndman, R.D., Chapman, R.N., Solem, R.C. & Lewis, T., 2006b. Geophysical and geochemical signatures associated with gas hydrate-related venting in the northern Cascadia margin, *GSA Bulletin,* **118**(1–2), 23–38.

Riedel, M., Trehu, A.M. & Spence, G.D., 2009. Characterizing the thermal regime of cold vents at the northern Cascadia margin from bottom-simulating reflector distributions, heat-probe measurements and borehole temperature data, *Mar. Geophys. Res.,* **31,** 1–16.

Sambridge, M., 2014. A Parallel Tempering algorithm for probabilistic sampling and multimodal optimization, *Geophys. J. Int.,* **196**(1), 357–374.

Sambridge, M., Bodin, T., Gallagher, K. & Tkalčić, H., 2013. Transdimensional inference in the geosciences, *Philosophical Transactions of the Royal Society A: Mathematical, Physical and Engineering Sciences,* **371**(1984), 20110547.

Scherwath, M., Riedel, M., Spence, G. & Hyndman, R., 2006. Data report. seismic structure beneath the north Cascadia drilling transect of IODP Expedition 311, in *Proceedings of the Integrated Ocean Drilling Program,* Vol. 311, pp. 1–25, eds Riedel, M., Collett, T., Malone, M. & the Expedition 311 Scientists, Integrated Ocean Drilling Program Management International, Inc., Washington, DC.

Scholl, C., 2005. The influence of multidimensional structures on the interpretation of LOTEM data with one-dimensional models and the application to data from Israel, *PhD thesis* at the University of Cologne.

Scholl, C., 2010. Resolving an Onshore Gas-hydrate Layer with Long-offset Transient Electromagnetics (LOTEM), in *Geophysical Characterization of Gas Hydrates,* pp. 149–162, eds Riedel, M., Willoughby, E.C. & Chopra, S., Society of Exploration Geophysicists.

Schwalenberg, K., 2007. Marine controlled source electromagnetics: Using a bottom-towed system to explore submarine cold vent sites in Cascadia and New Zealand, Presentation at IUGG 14th General Assembly.

Schwalenberg, K. & Engels, M., 2012. Marine controlled source electromagnetic methods for gas hydrate assessment: Latest results from the Black Sea and the Hikurangi Margin, NZ, Extended Abstract, 21st Workshop on Electromagnetic Induction in the Earth.

Schwalenberg, K., Willoughby, E., Mir, R.A. & Edwards, R.N., 2005. Marine gas hydrate electromagnetic signatures in Cascadia and their correlation with seismic blank zones, *First Break,* **23,** 99.

Schwalenberg, K., Haeckel, M., Poort, J. & Jegen, M., 2010a. Evaluation of gas hydrate deposits in an active seep area using marine controlled source electromagnetics: results from Opouawe Bank, Hikurangi Margin, New Zealand, *Marine Geology,* **272**(1–4), 89–98.

Schwalenberg, K., Wook, W., Pecher, I.A., Hamdan, L., Henrys, S., Jegen, M. & Coffin, R., 2010b. Preliminary interpretation of electromagnetic, heat flow, seismic, and geochemical data for gas hydrate distribution across the Porangahau Ridge, New Zealand, *Marine Geology,* **272**(1–4), 79–88.

Schwarz, G., 1978. Estimating the dimension of a model, *Ann. Stat.,* **6,** 461–464.

Steininger, G., Dettmer, J., Dosso, S. & Holland, C., 2013. Transdimensional joint inversion of seabed scattering and reflection data, *J. acoust. Soc. Am.,* **133**(3), 1347–1357.

Steininger, G., Dosso, S.E., Holland, C.W. & Dettmer, J., 2014. A transdimensional polynomial-spline parameterization for gradient-based geoacoustic inversion, *J. acoust. Soc. Am.,* **136**(4), 1563–1573.

Weitemeyer, K. & Constable, S., 2010. Mapping shallow geology and gas hydrate with marine CSEM surveys, *First Break,* **28,** 97–102.

Weitemeyer, K.A., Constable, S. & Tréhu, A.M., 2011. A marine electromagnetic survey to detect gas hydrate at Hydrate Ridge, Oregon, *Geophys. J. Int.,* **187**(1), 45–62.

Willoughby, E.C., Mir, R., Scholl, C. & Edwards, R.N., 2008. Neptune-Canada based Geophysical Imaging of Gas Hydrate in the Bullseye Vent, *Proceedings of the 6th International Conference on Gas Hydrates,* Vancouver, BC.

Yuan, J. & Edwards, R.N., 2000. The assessment of marine gas hydrates through electrical remote sounding: hydrate without a BSR?, *Geophys. Res. Lett.,* **27**(16), 2397–2400.

Yuan, T., Spence, G.D., Hyndman, R.D., Minshull, T.A. & Singh, S.C., 1999. Seismic velocity studies of a gas hydrate bottom-simulating reflector on the northern Cascadia continental margin: amplitude modeling and full waveform inversion, *J. geophys. Res.,* **104**(B1), 1179–1191.

Zühlsdorff, L. & Spiess, V., 2004. Three-dimensional seismic characterization of a venting site reveals compelling indications of natural hydraulic fracturing, *Geology,* **32,** 101–104.